Relation between oceanic plate structure, patterns of interplate locking and microseismicity in the 1922 Atacama Seismic Gap

Diego González-Vidal[1], Marcos Moreno[2], Christian Sippl[3], Juan Carlos Baez[4], Francisco H. Ortega-Culaciati[5], Dietrich Lange[6], Frederik Tilmann[7], Anne Socquet[8], Jan Bolte[9], Joaquin Hormazabal[10], Mickaël Langlais[11], Catalina Morales-Yáñez[12], Daniel Melnick[13], Roberto Benavente[14], and Rodolfo Araya[1]

[1]University of Concepción
[2]Pontifical Catholic University of Chile
[3]Institute of Geophysics, Czech Academy of Sciences
[4]UNIVERSIDAD DE CHILE
[5]Universidad de Chile
[6]Geomar, Helmholtz-Zentrum für Ozeanforschung Kiel
[7]Deutsches GeoForschungsZentrum GFZ
[8]Université Grenoble Alpes
[9]Kiel University
[10]University of Chile
[11]Univ. Grenoble Alpes, Univ. Savoie Mont Blanc, CNRS, IRD, Univ. Gustave Eiffel, ISTerre
[12]Universidad Católica de la Santísima Concepción
[13]Universidad Austral de Chile
[14]Universidad Catolica de la Santissima Concepcion

March 16, 2023

Abstract

We deployed a dense geodetic and seismological network in the Atacama seismic gap in Chile. We derive a microseismicity catalog of >30,000 events, time series from 70 GNSS stations, and apply a transdimensional Bayesian inversion to estimate interplate locking degree. We identify two highly locked regions of different sizes whose geometries appear to control seismicity patterns. Interface seismicity concentrates beneath the coastline just downdip of the highest locking. A region of lower interplate locking around 27.5ºS coincides with higher seismicity levels, a high number of repeating earthquakes and events extending further towards the trench. Having shown numerous signs of aseismic deformation (slow-slip events and earthquake swarms), this area is situated where the Copiapó Ridge is subducted. While these findings suggest that the structure of the downgoing oceanic plate prescribes patterns of interplate locking and seismicity, we note that the Taltal Ridge further north lacks a similar signature.

Relation between oceanic plate structure, patterns of interplate locking and microseismicity in the 1922 Atacama Seismic Gap

Diego González-Vidal[1], Marcos Moreno[2], Christian Sippl[3], Juan Carlos Baez[4], Francisco Ortega-Culaciati[5], Dietrich Lange[6], Frederik Tilmann[7,12], Anne Socquet[8], Jan Bolte[9], Joaquin Hormazabal[5], Mickael Langlais[8], Catalina Morales-Yáñez[10], Daniel Melnick[1], Roberto Benavente[10,11], Rodolfo Araya[13]

[1]Department of Earth Sciences, University of Concepción, Barrio Universitario s/n, 4030000 Concepció, Chile

[2]Department of Engineering and Geotectonic, Pontifical Catholic University of Chile, Av. Vicuña Mackenna 4860, 8331150 Santiago, Chile

[3]Institute of Geophysics, Czech Academy of Sciences, Bocni II/1401, 14131 Prague, Czech Republic

[4]National Seismological Center, Faculty of Physical and Mathematical Sciences, University of Chile, Av. Beaucheff 1225, 8370583 Santiago, Chile

[5]Department of Geophysics, Faculty of Physical and Mathematical Sciences, University of Chile, Av. Blanco Encalada 2002, 8370449 Santiago, Chile

[6]GEOMAR Helmholtz Centre for Ocean Research Kiel, Wischhofstrasse 1-3, 24098 Kiel, Germany

[7]Department of Geophysics, Deutsches GeoForschungsZentrum GFZ, Wissenschaftpark "Albert Einstein", Telegrafenberg, 14473 Potsdam, Germany

[8]Univ. Grenoble Alpes, Univ. Savoie Mont Blanc, CNRS, IRD, Univ. Gustave Eiffel, ISTerre, 38000 Grenoble, France

[9]Department of Mathematics, University of Kiel, Christian-Albrechts-Platz 4, 24118 Kiel, Germany

[10]Department of Civil Engineering, Universidad Católica de la Santísima Concepción, 4030000 Concepción, Chile

[11]National Research Center for Integrated Natural Disaster Management (CIGIDEN), 8370583 Santiago, Chile.

[12]Institute of Geological Sciences, Freie Universität Berlin, Kaiserswerther Str. 16-18, 14195 Berlin, Germany

[13]Departamento de Ingeniería Matemática & CI2MA, Universidad de Concepción, 4030000 Concepción, Chile

Corresponding author: Marcos Moreno, `marcos.moreno@ing.puc.cl`

Key Points:

- Microseismicity catalog and map of interplate locking derived for the Atacama 1922 seismic gap in North-Central Chile
- Plate interface seismicity coincides with downdip edge of high coupling
- Seismo-geodetic signals due to the subduction of the Copiapó ridge are prominent but negligible for the subducting Taltal Ridge.

Abstract

We deployed a dense geodetic and seismological network in the Atacama seismic gap in Chile. We derive a microseismicity catalog of >30,000 events, time series from 70 GNSS stations, and apply a transdimensional Bayesian inversion to estimate interplate locking degree. We identify two highly locked regions of different sizes whose geometries appear to control seismicity patterns. Interface seismicity concentrates beneath the coastline just downdip of the highest locking. A region of lower interplate locking around 27.5°S coincides with higher seismicity levels, a high number of repeating earthquakes and events extending further towards the trench. Having shown numerous signs of aseismic deformation (slow-slip events and earthquake swarms), this area is situated where the Copiapó Ridge is subducted. While these findings suggest that the structure of the downgoing oceanic plate prescribes patterns of interplate locking and seismicity, we note that the Taltal Ridge further north lacks a similar signature.

Plain Language Summary

Deformation along plate boundaries can occur seismically (i.e. through earthquakes) as well as aseismically (i.e. slipping slowly), and it is important to understand where each of these modes is dominant. Along the Chilean subduction contact, North-Central Chile is the only place where aseismic deformation episodes have been observed so far. In order to study these processes in detail, we deployed and operated dense geodetic and seismological networks in this region. Analyzing the data collected by these networks, we find notable relationships between seismic and aseismic processes. Thousands of small earthquakes are found at the boundaries of locked regions, whereas no small earthquakes are found at their interior. Thus, implying such regions are mechanically coupled, i.e. currently accumulating elastic deformation energy that will one day be released during a large earthquake. Along the North-Central Chilean plate boundary, there is one region (around 27.5°S) that shows many signs of aseismic deformation. It is located where a chain of seamounts is being subducted, which is likely responsible for the different behavior of this segment.

1 Introduction

Relative motion along the subduction zone plate interface is partitioned between seismic and aseismic processes (e.g. Perfettini et al., 2010). The seismogenic zone of the

megathrust accumulates slip deficit and releases it seismically during large earthquakes (Lay et al., 2012). In contrast, the adjacent updip and downdip regions tend to yield aseismic slip to account for part or the totality of the plate convergence(e.g. Peng & Gomberg, 2010). The amount of convergence accommodated in large earthquakes versus continuous or transient creep is highly variable along strike in many subduction zones (Métois et al., 2016). Different forms of aseismic slip are observed along the plate interface. Slow-slip events (SSEs) are days-to-months long aseismic slip pulses that usually occur at the downdip end of the plate interface and are often accompanied by non-volcanic tremor (Schwartz & Rokosky, 2007). However, SSEs have also been observed in the shallowest part of the plate interface (e.g., Araki et al., 2017) or within the seismogenic zone. Aseismic slip transients have also been observed to precede large earthquakes (e.g., Ito et al., 2013; Radiguet et al., 2016; Socquet et al., 2017; Voss et al., 2018), as a mixture of slow deformation and foreshocks (Bedford et al., 2015). Finally, aseismic slip unrelated to large earthquakes has also been observed along weakly locked segments of the plate interface. Increased seismicity rates or swarm-like sequences have been found to occur in direct vicinity to – and likely triggered by – aseismic transients (Vallée et al., 2013; Hirose et al., 2014). Repeating earthquakes, recurring small events that repeatedly rupture the same fault area, are thought to be a direct consequence of ongoing aseismic deformation in their surroundings (Igarashi et al., 2003; Uchida & Bürgmann, 2019).

SSEs along the Chilean margin appear to be rare or at least more subtle. North-Central Chile is one of the few sites where transient slow-slip events have been observed independently from large megathrust earthquakes in Chile. A SSE event of ∼18 months duration with a maximum slip of about 50 cm was observed at the deepest part of the plate interface in 2014 and 2015 (Klein, Duputel, et al., 2018), and again in 2020 (Klein et al., 2023). Swarm-like seismicity sequences have been observed in 2006 and 2015 close to the town of Caldera, updip of the SSE's location (Holtkamp et al., 2011; Ojeda et al., 2023), as well as ∼50-100 km further south in 2020 (Klein et al., 2021). However, this segment of the margin has until recently only been sparsely instrumented, so that a first more comprehensive analysis of its seismicity has only recently been undertaken (Pastén-Araya et al., 2022). The Atacama region was struck by a great ($Mw \sim 8.5$) earthquake in 1922 and by a similar event in 1819 (Fig. 1a), thus being considered a mature seismic gap, at risk of breaking in a great subduction earthquake (e.g., Yáñez-Cuadra et al., 2022).

In this study we deployed a dense network of 85 seismic stations complementing 16 stations already installed in the region (see Text S3, Figures 1, S6). Additionally, we deployed 28 continuous GNSS stations to densify the already existing network composed by 42 GNSS sites (see Text S1, Figures S1-S3). We created a high-resolution microseismicity catalog comprising more than 30,000 events occurring for 15 months since November 2020. We compare such seismicity to interplate locking constrained by GNSS secular rates and estimated using a transdimensional Bayesian approach. In this scheme, the spatial resolution of the locking model is obtained in a data-driven manner without the need for a priori smoothing. From these we derive constraints on the interplay of seismic and aseismic processes in the region. In the following sections, we first describe the derivation of the locking model from geodetic observations, as well as the seismicity catalog from the measured seismic waveforms.

2 A transdimentional Bayesian estimation of interplate locking

We used data from a total of 70 GNSS stations located between 23°S and 32°S, where two new deployments provided a total of 28 new stations in addition to the backbone network of the National Seismological Center of Chile (Figure 1; Table S1). We processed the GNSS data using Bernese software to produce daily positional time series for the period between January 2018 and February 2023 (Dach et al., 2015; Teunissen & Montenbruck, 2017; "VMF Data Server", 2021). Then, we clean the time series and adjust a trajectory model to isolate the secular velocity for each station in the ITRF2014 system (Huang et al., 2012; Bevis & Brown, 2014; Báez et al., 2018; Köhne et al., 2023). We refer the reader to Supplementary Text S1 for further details.

Over the analyzed period, no transient motions are visible in the raw time series or in the residuals of the trajectory model. The estimated horizontal velocities show a gradual increase north of 29°S (Figure 1b). Between 29°S and 31°S, a decrease in the magnitude of the velocities is observed in the area of the 2015 (M_w8.3) Illapel earthquake rupture (Figure 1a). Vertical motion shows subsidence at coastal stations at 27.2°S and 29°S, which may be related to changes in the depth of the locked zone.

We use the resulting velocities to estimate the degree of locking along the subduction megathrust based on the backslip model (Savage, 1983). We compute Green's functions accounting for interseismic viscoelastic relaxation using a finite element model, fol-

lowing the approach and rheological properties used by Aagaard et al. (2013); Li et al. (2015). The interseismic deformation field in the forearc of northern and central Chile is affected not only by contraction induced by plate coupling, but also by continental deformation driven by the partitioning of tectonic deformation along continental structures (e.g. Yáñez-Cuadra et al., 2022). Thus, to estimate the degree of locking, it is necessary to subtract the contribution of continental deformation from the regional displacement field. Therefore, we corrected the velocities by subtracting the predicted regional continental deformation tensor estimated by Yáñez-Cuadra et al. (2022) from the estimated displacements (Figure 1b). To estimate the degree of locking, we perform a Bayesian transdimensional inversion (Green, 1995; Bodin & Sambridge, 2009; Sambridge, 2013) where samples from the posterior probability function of backslip are obtained using the reversible jump Markov chain Monte Carlo (rj-MCMC) method. In our approach, the spatial distribution of locking is discretized by Voronoi cells (Dettmer et al., 2014). The number and location of Voronoi cell centers are not fixed, but are allowed to vary according to a stochastic process. We impose constraints of positivity and maximum fault slip along the up-dip direction (up-dip slip ≥ 0 and smaller than convergence rate between the tectonic plates). We note that this methodology follows Bayesian parsimony, where the size of the Voronoi cells slip discretization is driven by the resolving capability of the data and the properties of the physical model. Therefore, in contrast to typical least-squares optimization approaches that need some prior spatial smoothing constraint to solve the inherently ill-posed slip inversion (e.g., Ortega-Culaciati et al., 2021), our approach does not require such a subjective smoothing of the slip distribution (see Supplementary Text S2).

Using the transdimensional approach, we obtain an ensemble of more than 1 million locking models. From the ensemble, we compute the mean locking distribution shown in Figure 1b. The model fit well the horizontal and vertical observations (Figure S2) and shows a pattern of locking degree that increases northward, similar to the gradient shown by the surface displacement field. Our results show high values of interplate locking in the offshore region, with mostly lower values (<0.6) beneath the onshore regions. The margin north of 27.5°S appears to be highly locked, with the highest values around 26°S. A second smaller, less prominent locking high is situated in the south of the study area, around 28-29°S. It is separated from the northern locking high by a narrow region with a significantly lower locking degree around 27.7°S, where no values exceeding 0.5 are found.

Locking degree is very low in the southernmost part of the study region, possibly due to contamination with postseismic signals from the 2015 (M_w8.3) Illapel earthquake.

3 Seismicity catalog

We analyzed data from 101 seismic stations located in the Atacama seismic gap (24.4°S – 30.3°S) that continuously recorded waveforms from November 2020 to July 2022 (Figure 1). Given the large amount of data, we used an automated earthquake detection and location workflow based on machine learning techniques for phase picking (EQTransformer; Mousavi et al., 2019, 2020; Münchmeyer et al., 2022; Woollam et al., 2022) and phase association (GaMMA; Zhu et al., 2022). We define events as having at least 7 P- and 4 S-phases resulting in a seismicity catalog that features 30,560 events, comprising 469,980 P-phases and 391,350 S-phases. We then successively relocated this catalog based on a 1D as well as a 2D velocity model that was derived from a subset of our data (Kissling et al., 1994; Thurber & Eberhart-Phillips, 1999; Havskov et al., 2020), before eventually applying hypoDD (Waldhauser & Ellsworth, 2000) to obtain double-difference relocations (see Text S3). We estimate average location errors to be <5 km inside the network, while they increase to 10-25 km outside the network toward the trench and volcanic arc. Local magnitudes range from 0.6 to 5.7 and we obtain an overall completeness magnitude of 1.6 (Figure S9).

The seismicity catalog is presented in Figure 2. The apparent decay of seismicity north of ∼24.5°S and south of ∼29.5°S is likely due to the lower detection capability plus shorter deployment times in such regions. A continuous band of high background seismicity beneath the coastline is the most prominent feature of the catalog. Events in this band, located ∼30-100 km from the trench, define two parallel planes with <10 km vertical separation in profile view (Figure 2b-e). While the upper plane likely corresponds to the deeper portion of the plate interface, its deepest (¿ ∼75 km) portion is located inside the downgoing slab and corresponds to the upper band of an occasionally visible double seismic zone (DSZ, e.g. Brudzinski et al., 2007; Sippl et al., 2018). Seismicity is scarce at the shallower part of the plate interface, extending closer to the trench along a total of four or five narrow features (Figure 2a), that also host significant concentrations of repeating earthquakes (see Text S4). Seawards of the trench, scattered events south of 26°S likely occurred in the outer rise region. Due to their location far outside the network, the depth of these events is very badly defined. East of the coastline, seis-

micity is largely found inside the downgoing slab, confined to the uppermost 25-30 km of the lithosphere. Most of this intraslab seismicity occurs at ∼50-120 km depth, between ∼150-300 km distance from the trench. The geometry and vigor of intraslab seismicity is highly variable along strike. In the north (Figure 2b), most seismicity occurs in the uppermost 10-15 km of the slab, whereas deeper levels (20-30 km below slab surface) are most active further south (Figure 2d,e). In profiles c and d of Figure 2, a clear DSZ with about 15 km separation between both bands is visible. The southward transition to the Pampean flat slab is accompanied by high seismicity levels deeper within the downgoing slab. We obtain 3,431 upper plate seismic events, defined as those located at <15 km depth and >5 km above the top of the subducted slab. Their occurrence rate is significantly increased during local daytime, suggesting a predominance of mining blast activity (Figure S10).

4 Discussion

4.1 Relation between microseismicity and interplate locking

Figure 3 summarizes the spatial relationship between interplate locking and the occurrence of microseismicity along the North-Central Chile margin. The highest concentration of microseismicity is found to occur just seawards and beneath the coastline (Figure 3a), with hypocentral depths between ∼25 and 40 km. This location roughly corresponds to the landward edge of the highly locked regions, indicating that most seismicity occurs where locking starts to decrease in the downdip direction (Figure 3c). In contrast, the shallow part of the megathrust is largely aseismic, and most seismicity that extends further towards the trench is confined to a weakly locked region between ∼27.5 and 28°S. When projected in the along-strike direction (Figure 3b), the highest seismicity concentrations and the largest number of repeating earthquakes (Uchida & Matsuzawa, 2013) can be found along the northern and southern terminations of the southern highly locked patch.

A very similar pattern of seismicity and interplate locking was found just south of the study region (Sippl et al., 2021), where it was interpreted as the signature of mature asperities on the megathrust. Accumulation of convergence over most of the seismic cycle creates a "halo" of high stresses around the downdip edge of highly locked regions (e.g. Moreno et al., 2018; Schurr et al., 2020). This "halo" may be the cause of the high

levels of background seismicity we observe on the deeper part of the plate interface. The weak locking and high seismicity we obtain around 27.7°S likely represents a segment of the megathrust that features more aseismic deformation. Weak locking in this location is a stable feature across all published locking maps of the area (Métois et al., 2016; Klein, Métois, et al., 2018; Yáñez-Cuadra et al., 2022), and numerous indicators for slow slip processes have been observed here (Section 4.2; Figure 4). The seismicity in the shallower part of the plate interface in this region is probably driven by such slow slip processes, which explains its absence in other, more highly locked regions of the megathrust.

The southern termination of the southern locked patch around 29°S features increased seismicity levels and elevated numbers of repeating earthquakes (Figure 2), similar to the region around 27.7°S. While the resolution of our catalog is very low south of ∼29°S, Sippl et al. (2021) shows an extended zone of increased shallow plate interface seismicity up to ∼30.5°S. This could hint the presence of aseismic processes related to the incoming Challenger Fracture Zone (Figures 1a and 3), which is thought to have prescribed the northern termination of the 2015 M_w 8.3 Illapel earthquake (e.g., Tilmann et al., 2016; Poli et al., 2017).

4.2 Seismic and aseismic signature of the Copiapó Ridge

Figure 4 summarizes observations of seismic and aseismic processes in the vicinity of the incoming Copiapó Ridge. A prominent offshore seismic swarm occurred in the region in 2006 (Holtkamp et al., 2011), and similar swarm occurrences have been reported for the years 1973, 1979 and 2015 (e.g., Ojeda et al., 2023). The 2014 SSE was situated further downdip but covered the same latitudinal range (Klein, Duputel, et al., 2018). A similar SSE was identified starting in March 2020, confined to the southern part of the 2014 SSE (Klein et al., 2023). Aseismic slip continued at least until September 2020, when the Atacama seismic sequence (see below) began to shadow the SSE signal. Non-volcanic tremor events observed in 2019 (Pastén-Araya et al., 2022) occurred directly updip of the 2014 SSE. In September 2020, only 2.5 months before the start of our catalog and GNSS observations, the Atacama seismic sequence occurred, featuring three major earthquakes of M>6. In addition, unusually large amounts of aseismic slip, equivalent to M_w 6.8, occurred within the weakly coupled patch between the mainshock of the Atacama seismic sequence and the southern edge of the 2014 SSE (Klein et al., 2021).

This sequence was situated along the southern edge of our inferences of weak locking, whereas all previously mentioned observations of earthquake swarms, SSEs and NVTs were situated 50-100 km further north (Figure 4). We found continued elevated background seismicity rates throughout the studied time interval in the latitudinal range of the 2020 Atacama sequence, accompanied by some repeating earthquakes (Figure 2).

Taken together, all these observations highlight the complex interplay of seismic and aseismic processes in the direct vicinity of the subduction of the Copiapó Ridge. It has previously been shown that elevated roughness on the downgoing plate leads to reduced interplate coupling (Wang & Bilek, 2014), as well as the formation of weakly coupled, creeping segments that may act as "barriers" to large earthquakes due to the lack of stress accumulation. Subducting ridges have also been shown to feature enhanced hydration of the downgoing plate, which can further reduce interplate coupling through the release of fluids and the subsequent increase of pore fluid pressure on the plate interface (e.g. Moreno et al., 2014). While these observations suggest that the region around 27.7°S represents a weakly locked "barrier" that may hinder the propagation of large megathrust earthquakes, the two last major earthquakes in 1922 and 1819 have both ruptured across it (Figure 1a). North of 26°S, the Taltal Ridge impinges onto the North-Central Chilean margin. Although its offshore bathymetric expression is similar to the Copiapó Ridge (Figure 1), we do not retrieve a region of lower interplate locking degree or elevated seismicity in this region (Figures 1 and 3). Whether this implies that the Taltal Ridge has only recently started to be subducted, or whether it possesses properties that clearly distinguish it from the Copiapó Ridge, is currently unclear.

4.3 Intraslab seismicity

Here we only provide a brief general overview of intraslab seismicity, with a more detailed analysis delegated to a future study. Our catalog shows Nazca plate intraslab seismicity occurring at depths ranging 35-∼120 km. A DSZ can be recognized, with its upper seismicity band most vigorously active directly beneath where most plate interface seismicity occurs (Figure 2c). The lower band of the DSZ, located ∼15 km below the upper band, within the downgoing slab, shows only weak activity at depths shallower than 80 km. At larger depths, seismicity in deeper levels of the slab intensifies. Thus, being harder to distinguish the two bands of the DSZ, as seismicity fills the gap between the two zones, in a similar manner as independent observations in Northern Chile (e.g.

Sippl et al., 2018). Most of this deeper intraslab seismicity is concentrated south of 27°S, with a clear maximum around 27.4°S. Intraslab earthquakes at intermediate depths are thought to be related to dehydration processes in the downgoing oceanic lithosphere (e.g. Hacker et al., 2003; Zhan, 2020). It is widely assumed that the loci and rate of seismicity in the slab represent the distribution of fluid release at depth. The concentration of deeper seismicity around 27.4°S may be the signature of increased hydration of the downgoing Copiapó Ridge. Streaks of increased intermediate-depth seismicity have been previously shown along the trace of downgoing ocean features along the Chilean margin (e.g. Kirby et al., 1996; Geersen et al., 2022). We could hypothesize there is a direct causal link between the different signatures of the Copiapó Ridge on the plate interface (low locking degree and seismicity) and within the slab (increased seismicity), through fluid processes, for instance. Alternatively, both behaviors may be independent consequences of ridge subduction. Discriminating between these hypotheses is beyond the scope of this contribution. We note that the signature of the Taltal Ridge further north is again less clearly visible, if present at all.

5 Conclusions

We combine novel highly resolved seismological and geodetic observations and model these using frontier techniques. Our results identify a number of distinct seismic and aseismic patterns that appear to be mainly influenced by the structure of the downgoing Nazca Plate. Our inferred locking distribution suggests that the Atacama seismic gap consists of two highly coupled regions of different sizes, separated by a creeping corridor with higher background seismicity. The geometry of these two "asperities" appears to control seismicity patterns. While the highly locked shallow part of the plate interface presents scarce seismicity, the downdip limit of interplate locking is marked by a band of background seismicity located beneath the coastline. Interplate locking decreases significantly around 27.7°S, where seismicity reaches shallower depths and numerous indicators for ongoing aseismic slip processes have been observed. The subduction of the Copiapó Ridge at this latitude creates a clear signature along the megathrust and at deeper depths inside the downgoing slab, both as a consequence of bathymetric roughness and/or increased (de)hydration.

Acknowledgments

Field work and instrumentation were funded by the ANILLO ACT192169 grant, ERC Deep-Trigger 865963 project and GFZ-Potsdam. M. M., D. G.V.,J.C. B., F. O.C., J.H., C.M.Y., D.M., R.B. acknowledge support from the ANILLO Precursor grant ACT192169. M.M., D.M. acknowledges FONDECYT 1221507 and the Millennium Nucleus "The Seismic Cycle Along Subduction Zones" grant NC160025. C.S. received funding from the European Research Council (ERC) through the Horizon 2020 program (ERC Starting Grant MILESTONE; StG2020-947856). C. M.Y. acknowledges support from FONDECYT 3220307. A.S. received funding from the European Research Council (ERC) CoG 865963 DEEP-trigger. Finally, we thank the GFZ Potsdam GIPP, B. Heit and the French national pool of portable seismic instruments SISMOB-RESIF (INSU-CNRS) for providing the seismological instruments and related metadata used in this study. Powered@NLHPC: This research was partially supported by the supercomputing infrastructure of the NLHPC (ECM-02).

Author Contribution

Experiment design: F. Tilmann, M. Moreno, J.C. Baez, F. Ortega-Culaciati, A. Socquet, M. Langlais, D. Melnick

Funding acquisition: F. Tilmann, M. Moreno, F. Ortega-Culaciati, A. Socquet, D. Melnick.

Methodology: D. González-Vidal, C. Sippl, M. Moreno, D. Lange, J.C. Baez, F. Ortega-Culaciati.

Software: J. Bolte, M. Moreno, J.C. Baez, F. Ortega-Culaciati, C. Sippl, D. Lange.

Analysis of seismic data: D. González-Vidal, C. Sippl, D. Lange, C. Morales.

Analysis of GNSS data: M. Moreno, J.C. Baez, F. Ortega-Culaciati.

Figures: D. González-Vidal, C. Sippl, M. Moreno.

Writing - original draft: C. Sippl, M. Moreno, D. González-Vidal, J.C. Baez.

Writing - review and editing: everyone

Data Availability

The seismic waveforms we used in this paper to compile the earthquake catalog was retrieved from the GEOFON data centre of the GFZ German Research Centre for Geosciences and IRIS Web, and come from the networks Y6 (Tilmann et al., 2021), XZ (Socquet

et al., 2025), CX (GFZ & CNRS-INSU, 2006), C1 (Universidad de Chile, 2013), C (https://www.fdsn.org/network and IU (Albuquerque Seismological Laboratory/USGS (ASL), 2014). XZ data are archived at the EPOS-FRANCE RESIF data center (https://seismology.resif.fr/fr/reseaux/#/XZ_2020) and will be opened at the end of the project (2026). Moment tensors used in Figure 4 were retrieved from the GEOFON program of the GFZ German Research Centre for Geosciences (https://geofon.gfz-potsdam.de/eqinfo/). The earthquake catalog, GNSS time series and locking model presented in this article will be available as a data publication at the GFZ Data Center at https://nextcloud.gfz-potsdam.de/s/oGAbANpe2jQiBzd (temporary link; the dataset will be archived at GFZ data services and a DOI issued for it after taking into account reviewer comments).

References

Aagaard, B. T., Knepley, M. G., & Williams, C. A. (2013). A domain decomposition approach to implementing fault slip in finite-element models of quasi-static and dynamic crustal deformation. *Journal of Geophysical Research: Solid Earth*, *118*(6), 3059-3079. Retrieved from `https://agupubs.onlinelibrary.wiley.com/doi/abs/10.1002/jgrb.50217` doi: 10.1002/jgrb.50217

Albuquerque Seismological Laboratory/USGS (ASL). (2014). *Global Seismograph Network (GSN - IRIS/USGS) [Dataset].* Federation of Digital Seismograph Networks. doi: https://doi.org/10.7914/SN/IU

Araki, E., Saffer, D., Kopf, A. J., Wallace, L., Kimura, T., Machida, Y., ... Davis, E. (2017). Recurring and triggered slow-slip events near the trench at the Nankai Trough subduction megathrust. *Science*, *356*(6343), 1157–1160. doi: 10.1126/science.aan3120

Barrientos, S. (2018). The Seismic Network of Chile. *Seismological Research Letters*, *89*(2A), 467–474. doi: 10.1785/0220160195

Bedford, J., Moreno, M., Schurr, B., Bartsch, M., & Oncken, O. (2015). Investigating the final seismic swarm before the iquique-pisagua 2014 mw 8.1 by comparison of continuous gps and seismic foreshock data. *Geophysical Research Letters*, *42*(10), 3820-3828. doi: https://doi.org/10.1002/2015GL063953

Bevis, M., & Brown, A. (2014). Trajectory models and reference frames for crustal motion geodesy. *Journal of Geodesy*, *88*, 283–311. doi: 10.1007/s00190-013

-0685-5

Bodin, T., & Sambridge, M. (2009). Seismic tomography with the reversible jump algorithm. *Geophysical Journal International*, *178*, 1411-1436.

Brudzinski, M. R., Thurber, C. H., Hacker, B. R., & Engdahl, E. R. (2007). Global prevalence of double benioff zones. *Science*, *316*(5830), 1472–1474. doi: 10.1126/science.1139204

Báez, J. C., Leyton, F., Troncoso, C., del Campo, F., Bevis, M., Vigny, C., ... Blume, F. (2018). The Chilean GNSS Network: Current Status and Progress toward Early Warning Applications. *Seismological Research Letters*, *89*(4), 1546-1554. doi: 10.1785/0220180011

Dach, R., Lutz, S., Walser, P., & Fridez, P. e. (2015). Bernese GNSS Software Version 5.2. In *University of Bern, Bern Open Publishing.* doi: 10.7892/boris.72297

Dettmer, J., Benavente, R., Cummins, P. R., & Sambridge, M. (2014). Trans-dimensional finite-fault inversion. *Geophysical Journal International*, *199*(2), 735-751. doi: 10.1093/gji/ggu280

Geersen, J., Sippl, C., & Harmon, N. (2022). Impact of bending-related faulting and oceanic-plate topography on slab hydration and intermediate-depth seismicity. *Geosphere*, *18*(2), 562–584. doi: https://doi.org/10.1130/GES02367.1

GFZ, & CNRS-INSU. (2006). *IPOC Seismic Network: Integrated Plate boundary Observatory Chile - IPOC.* GFZ Data Services. doi: 10.14470/PK615318

Green, P. J. (1995). Reversible jump Markov chain Monte Carlo computation and Bayesian model determination. *Biometrika*, *82*, 711-732.

Hacker, B. R., Peacock, S. M., Abers, G. A., & Holloway, S. D. (2003). Subduction factory 2. Are intermediate-depth earthquakes in subducting slabs linked to metamorphic dehydration reactions? *Journal of Geophysical Research*, *108*(B1). doi: 10.1029/2001JB001129

Havskov, J., Voss, P. H., & Ottemöller, L. (2020, 03). Seismological Observatory Software: 30 Yr of SEISAN. *Seismological Research Letters*, *91*(3), 1846-1852. doi: 10.1785/0220190313

Hayes, G. P., Moore, G., Portner, D. E., Hearne, M., Flamme, H., Furtney, M., & Smoczyk, G. M. (2018). Slab2, a comprehensive subduction zone geometry model. *Science*, *362*(6410), 58–61. doi: 10.1126/science.aat4723

Hirose, H., Matsuzawa, T., Kimura, T., & Kimura, H. (2014). The Boso slow slip events in 2007 and 2011 as a driving process for the accompanying earthquake swarm. *Geophysical Research Letters*, *41*(8), 2778–2785. doi: 10.1002/2014GL059791

Holtkamp, S. G., Pritchard, M. E., & Lohman, R. B. (2011). Earthquake swarms in South America. *Geophysical Journal International*, *187*(1), 128–146.

Huang, D., Dai, W., & Luo, F. (2012, 10). Ica spatiotemporal filtering method and its application in gps deformation monitoring. *Applied Mechanics and Materials*, *204-208*, 2806-2812. doi: 10.4028/www.scientific.net/AMM.204-208.2806

Igarashi, T., Matsuzawa, T., & Hasegawa, A. (2003). Repeating earthquakes and interplate aseismic slip in the northeastern Japan subduction zone. *Journal of Geophysical Research: Solid Earth*, *108*(B5), 1–9. doi: 10.1029/2002jb001920

Ito, Y., Hino, R., Kido, M., Fujimoto, H., Osada, Y., Inazu, D., ... Ashi, J. (2013). Episodic slow slip events in the japan subduction zone before the 2011 tohoku-oki earthquake. *Tectonophysics*, *600*, 14-26. doi: https://doi.org/10.1016/j.tecto.2012.08.022

Kirby, S., Engdahl, E. R., & Denlinger, R. (1996). Intermediate-depth intraslab earthquakes and arc volcanism as physical expressions of crustal and uppermost mantle metamorphism in subducting slabs. *Geophysical Monograph Series*, *96*, 195–214. doi: 10.1029/GM096p0195

Kissling, E., Ellsworth, W. L., Eberhart-Phillips, D., & Kradolfer, U. (1994). Initial reference models in local earthquake tomography. *Journal of Geophysical Research*, *99*(B10), 19,635–19,646.

Klein, E., Duputel, Z., Zigone, D., Vigny, C., Boy, J. P., Doubre, C., & Meneses, G. (2018). Deep Transient Slow Slip Detected by Survey GPS in the Region of Atacama, Chile. *Geophysical Research Letters*, *45*(22), 12,263–12,273. doi: 10.1029/2018GL080613

Klein, E., Métois, M., Meneses, G., Vigny, C., & Delorme, A. (2018). Bridging the gap between North and Central Chile: Insight from new GPS data on coupling complexities and the Andean sliver motion. *Geophysical Journal International*, *213*(3), 1924–1933. doi: 10.1093/gji/ggy094

Klein, E., Potin, B., Pasten-Araya, F., Tissandier, R., Azua, K., Duputel, Z., ... Vigny, C. (2021). Interplay of seismic and a-seismic deformation during the

2020 sequence of Atacama , Chile. *Earth and Planetary Science Letters*, *570*, 117081. doi: 10.1016/j.epsl.2021.117081

Klein, E., Vigny, C., Duputel, Z., Zigone, D., Rivera, L., Ruiz, S., & Potin, B. (2023). Return of the Atacama deep Slow Slip Event: The 5-year recurrence confirmed by continuous GPS. *Physics of the Earth and Planetary Interiors*, *334*, 106970. doi: 10.1016/j.pepi.2022.106970

Köhne, T., Riel, B., & Simons, M. (2023). Decomposition and inference of sources through spatiotemporal analysis of network signals: The disstans python package. *Computers & Geosciences*, *170*, 105247. doi: https://doi.org/10.1016/j.cageo.2022.105247

Lay, T., Kanamori, H., Ammon, C. J., Koper, K. D., Hutko, A. R., Ye, L., ... Rushing, T. M. (2012). Depth-varying rupture properties of subduction zone megathrust faults. *Journal of Geophysical Research*, *117*(4), B04311. doi: 10.1029/2011JB009133

Li, S., Moreno, M., Bedford, J., Rosenau, M., & Oncken, O. (2015). Revisiting viscoelastic effects on interseismic deformation and locking degree: A case study of the peru-north chile subduction zone. *Journal of Geophysical Research: Solid Earth*, *120*(6), 4522-4538. doi: https://doi.org/10.1002/2015JB011903

Métois, M., Vigny, C., & Socquet, A. (2016). Interseismic Coupling, Megathrust Earthquakes and Seismic Swarms Along the Chilean Subduction Zone (38°–18°S). *Pure and Applied Geophysics*, *173*(5), 1431–1449. doi: 10.1007/s00024-016-1280-5

Moreno, M., Haberland, C., Oncken, O., Rietbrock, A., Angiboust, S., & Heidbach, O. (2014). Locking of the Chile subduction zone controlled by fluid pressure before the 2010 earthquake. *Nature Geoscience*, *7*(4), 292–296. doi: 10.1038/ngeo2102

Moreno, M., Li, S., Melnick, D., Bedford, J., Baez, J. C., Motagh, M., ... Oncken, O. (2018). Chilean megathrust earthquake recurrence linked to frictional contrast at depth. *Nature Geoscience*, *11*(4), 285–290. doi: 10.1038/s41561-018-0089-5

Mousavi, S. M., Ellsworth, W. L., Zhu, W., Chuang, L. Y., & Beroza, G. C. (2020). Earthquake transformer—an attentive deep-learning model for simultaneous earthquake detection and phase picking. *Nature Communications*, *11*. doi:

10.1038/s41467-020-17591-w

Mousavi, S. M., Sheng, Y., Zhu, W., & Beroza, G. C. (2019). STanford EArthquake Dataset (STEAD): A Global Data Set of Seismic Signals for AI. *IEEE Access*, *7*, 179464–179476. Retrieved from `http://dx.doi.org/10.1109/ACCESS.2019.2947848` doi: 10.1109/access.2019.2947848

Münchmeyer, J., Woollam, J., Rietbrock, A., Tilmann, F., Lange, D., Bornstein, T., ... Soto, H. (2022). Which picker fits my data? a quantitative evaluation of deep learning based seismic pickers. *Journal of Geophysical Research: Solid Earth*, *127*. doi: 10.1029/2021JB023499

Ojeda, J., Morales-Yáñez, C., Ducret, G., Ruiz, S., Grandin, R., Doin, M.-P., ... Nocquet, J.-M. (2023). Seismic and aseismic slip during the 2006 Copiapo swarm in North-Central Chile. *Journal of South American Earth Sciences*, 104198. doi: 10.1016/j.jsames.2023.104198

Ortega-Culaciati, F., Simons, M., Ruiz, J., Rivera, L., & Díaz-Salazar, N. (2021). An epic tikhonov regularization: Application to quasi-static fault slip inversion. *Journal of Geophysical Research: Solid Earth*, *126*(7), e2020JB021141. doi: 10.1029/2020JB021141

Pastén-Araya, F., Potin, B., Azúa, K., Sáez, M., Aden-Antoniów, F., Ruiz, S., ... Duputel, Z. (2022). Along-Dip Segmentation of the Slip Behavior and Rheology of the Copiapó Ridge Subducted in North-Central Chile. *Geophysical Research Letters*(49), e2021GL095471. doi: 10.1029/2021gl095471

Peng, Z., & Gomberg, J. (2010). An integrated perspective of the continuum between earthquakes and slow-slip phenomena. *Nature Geoscience*, *3*(9), 599–607. doi: 10.1038/ngeo940

Perfettini, H., Avouac, J.-P., Tavera, H., Kositsky, A., Nocquet, J. M., Bondoux, F., ... Soler, P. (2010). Seismic and aseismic slip on the Central Peru megathrust. *Nature*, *465*(7294), 78–81. doi: 10.1038/nature09062

Poli, P., Jeria, A. M., & Ruiz, S. (2017). The Mw 8.3 lllapel earthquake (Chile): Preseismic and postseismic activity associated with hydrated slab structures. *Geology*, *45*(3), 247–250. doi: 10.1130/G38522.1

Radiguet, M., Perfettini, H., Cotte, N., Gualandi, A., Valette, B., Kostoglodov, V., ... Campillo, M. (2016). Triggering of the 2014 m w 7.3 papanoa earthquake by a slow slip event in guerrero, mexico. *Nature Geoscience*, *9*(11), 829–833.

Sambridge, M. (2013, 10). A Parallel Tempering algorithm for probabilistic sampling and multimodal optimization. *Geophysical Journal International*, *196*(1), 357-374. doi: 10.1093/gji/ggt342

Savage, J. C. (1983). A dislocation model of strain accumulation and release at a subduction zone. *Journal of Geophysical Research: Solid Earth*, *88*(B6), 4984-4996. doi: https://doi.org/10.1029/JB088iB06p04984

Schurr, B., Moreno, M., Tréhu, A. M., Bedford, J., Kummerow, J., Li, S., & Oncken, O. (2020). Forming a Mogi Doughnut in the Years Prior to and Immediately Before the 2014 M8.1 Iquique, Northern Chile, Earthquake. *Geophysical Research Letters*, *47*(16). doi: 10.1029/2020GL088351

Schwartz, S. Y., & Rokosky, J. M. (2007). Slow slip events and seismic tremor at circum-pacific subduction zones. *Reviews of Geophysics*, *45*(3), RG3004. doi: 10.1029/2006RG000208

Sippl, C., Moreno, M., & Benavente, R. (2021). Microseismicity appears to outline highly coupled regions on the Central Chile megathrust. *Journal of Geophysical Research: Solid Earth*, *126*, e2021JB022252. doi: 10.1029/2021jb022252

Sippl, C., Schurr, B., Asch, G., & Kummerow, J. (2018). Seismicity structure of the northern chile forearc from >100,000 double-difference relocated hypocenters. *Journal of Geophysical Research: Solid Earth*, *123*, 4063-4087. doi: 10.1002/2017JB015384

Socquet, A., Baez, J. C., Moreno, M., Langlais, M., & DEEP-Trigger Team and Geophysics Technical Service at ISTerre and RESIF. (2025). *DEEP-TRIGGER temporary experiment in the subduction zone Peru/Chile, Chile.* RESIF - Réseau Sismologique et géodésique Français. doi: 10.15778/RESIF.XZ2020

Socquet, A., Valdes, J. P., Jara, J., Cotton, F., Walpersdorf, A., Cotte, N., ... Norabuena, E. (2017). An 8 month slow slip event triggers progressive nucleation of the 2014 Chile megathrust. *Geophysical Research Letters*, *44*(9), 4046–4053. doi: 10.1002/2017GL073023

Tassara, A., & Echaurren, A. (2012). Anatomy of the Andean subduction zone: Three-dimensional density model upgraded and compared against global-scale models. *Geophysical Journal International*, *189*, 161–168.

Teunissen, P. J., & Montenbruck, O. (2017). *Springer Handbook of Global Navigation Satellite Systems.* Springer Cham. doi: https://doi.org/10.1007/978-3-319

-42928-1

Thurber, C. H., & Eberhart-Phillips, D. (1999). Local earthquake tomography with flexible gridding. *Computers and Geosciences*, *25*(7), 809–818. doi: 10.1016/S0098-3004(99)00007-2

Tilmann, F., Heit, B., Moreno, M., & González-Vidal, D. (2021). *Anillo.* GFZ Data Services. doi: 10.14470/L17575324477

Tilmann, F., Zhang, Y., Moreno, M., Saul, J., Eckelmann, F., Palo, M., ... Dahm, T. (2016). The 2015 Illapel earthquake, central Chile: a type case for a characteristic earthquake ? *Geophysical Research Letters*, *43*, 574–583. doi: 10.1002/2015GL066963

Uchida, N., & Bürgmann, R. (2019). Repeating Earthquakes. *Annual Review of Earth and Planetary Sciences*, *47*(1), 305–332. doi: 10.1146/annurev-earth-053018-060119

Uchida, N., & Matsuzawa, T. (2013). Pre- and postseismic slow slip surrounding the 2011 Tohoku-oki earthquake rupture. *Earth and Planetary Science Letters*, *374*, 81-91. doi: 10.1016/j.epsl.2013.05.021

Universidad de Chile. (2013). *Red Sismologica Nacional. International Federation of Digital Seismograph Networks.* doi: https://doi.org/10.7914/SN/C1

Vallée, M., Nocquet, J. M., Battaglia, J., Font, Y., Segovia, M., Régnier, M., ... Chlieh, M. (2013). Intense interface seismicity triggered by a shallow slow slip event in the Central Ecuador subduction zone. *Journal of Geophysical Research: Solid Earth*, *118*(6), 2965–2981. doi: 10.1002/jgrb.50216

VMF Data Server. (2021). In *re3data.org: Vmf data server; editing status 2021-08-24; re3data.org - registry of research data repositories.* doi: http://doi.org/10.17616/R3RD2H

Voss, N., Dixon, T. H., Liu, Z., Malservisi, R., Protti, M., & Schwartz, S. (2018). Do slow slip events trigger large and great megathrust earthquakes? *Science advances*, *4*(10), eaat8472.

Waldhauser, F., & Ellsworth, W. L. (2000). A Double-difference Earthquake location algorithm: Method and application to the Northern Hayward Fault, California. *Bulletin of the Seismological Society of America*, *90*(6), 1353–1368. doi: 10.1785/0120000006

Wang, K., & Bilek, S. L. (2014). Invited review paper: Fault creep caused by sub-

duction of rough seafloor relief. *Tectonophysics*, *610*, 1–24. doi: 10.1016/j.tecto .2013.11.024

Woollam, J., Münchmeyer, J., Tilmann, F., Rietbrock, A., Lange, D., Bornstein, T., ... Soto, H. (2022). SeisBench—A Toolbox for Machine Learning in Seismology. *Seismological Research Letters*, *93*(3), 1695-1709. doi: 10.1785/0220210324

Yáñez-Cuadra, V., Ortega-Culaciati, F., Moreno, M., Tassara, A., Krumm-Nualart, N., Ruiz, J., ... Benavente, R. (2022). Interplate Coupling and Seismic Potential in the Atacama Seismic Gap (Chile): Dismissing a Rigid Andean Sliver. *Geophysical Research Letters*, 1–26. doi: 10.1029/2022gl098257

Zhan, Z. (2020). Mechanisms and Implications of Deep Earthquakes. *Annual Review of Earth and Planetary Sciences*, *48*, 147–174. doi: 10.1146/annurev -earth-053018-060314

Zhu, W., McBrearty, I. W., Mousavi, S. M., Ellsworth, W. L., & Beroza, G. C. (2022). Earthquake phase association using a bayesian gaussian mixture model. *Journal of Geophysical Research: Solid Earth*, *127*(5), e2021JB023249. (e2021JB023249 2021JB023249) doi: https://doi.org/10.1029/2021JB023249

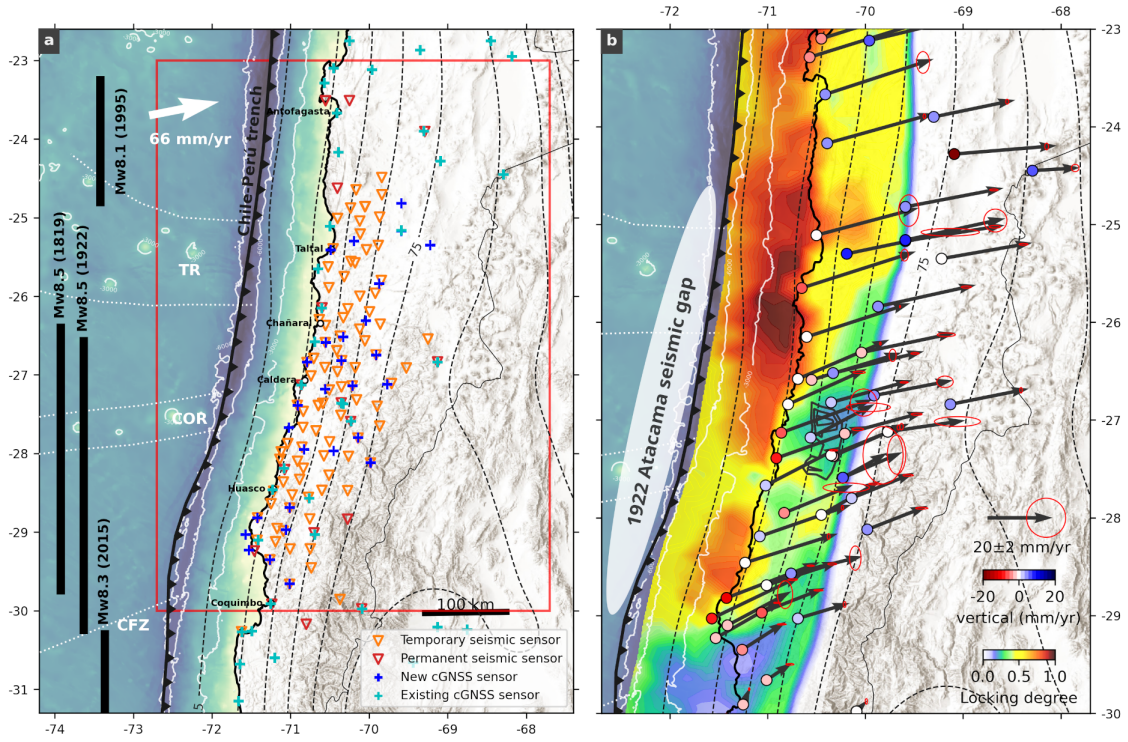

Figure 1. (a) Map view showing the distribution of existing and new GNSS and seismic networks in North-central Chile. The slab surface after model slab2 (Hayes et al., 2018) is shown with dashed black contour lines at 15 km intervals, the black barbed line marks the Chile-Perú trench and the white dotted outlines show prominent seafloor features (CFZ - Challenger Fracture Zone; COR - Copiapó Ridge; TR - Taltal Ridge). Rupture extents of historical megathrust earthquakes (M>8) are shown on the left. The red rectangle shows the extent of subfigure b). (b) Horizontal (vectors) and vertical (point coloring) velocities and uncertainties (red ellipses) of GNSS stations used in this study, shown together with the derived mean interplate locking model. The extent of the 1922 Atacama seismic gap is shown by the white ellipse on the left.

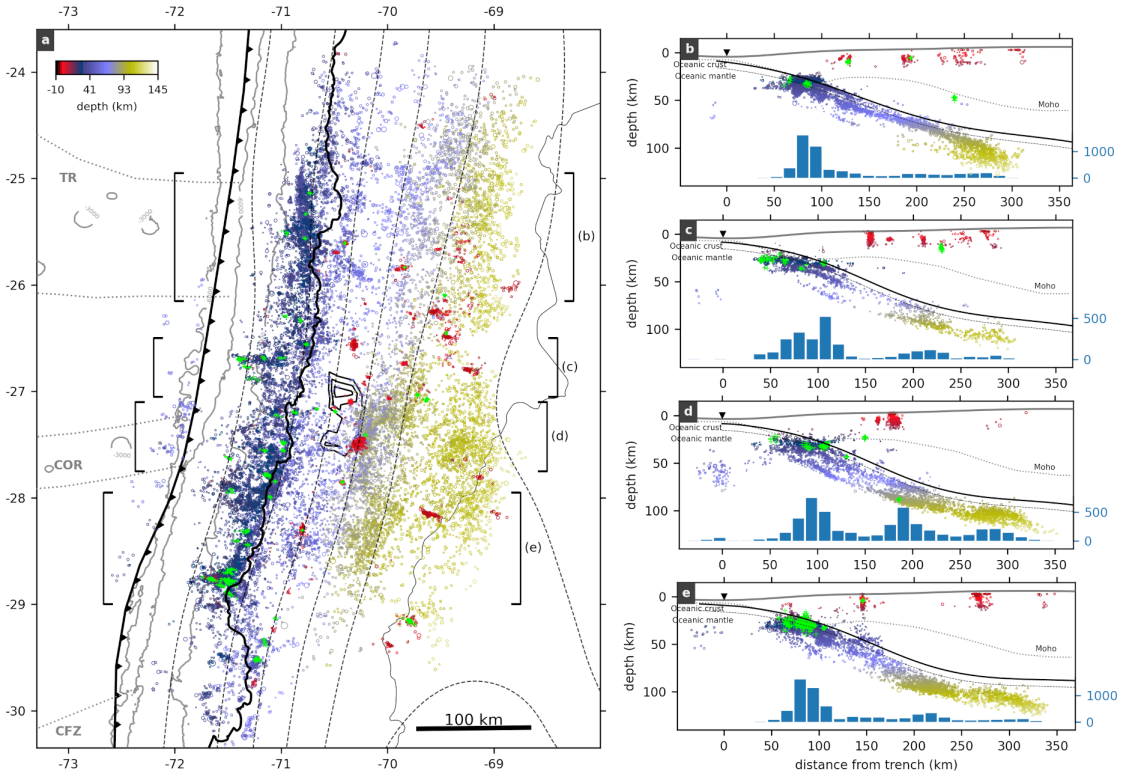

Figure 2. Map view (a) and profile projections (b-e) of the 30,560 hypocenters in the seismicity catalog, color-coded by depth. Families of repeaters are shown by green plus markers. The locations and swath widths of the profile projections are indicated by the black brackets in subfigure a). The black barbed line in the map view plot marks the location of the trench, the dotted pale grey lines show prominent seafloor features. The slab2 slab surface (Hayes et al., 2018) is shown with dashed contour lines in a) and with solid lines in the profile plots. The dashed black line in the profiles shows the inferred oceanic Moho located 7km below the slab2 surface. The dotted thin line shows the continental Moho from Tassara and Echaurren (2012). The position of the trench is marked by black inverted triangles. The blue histograms show earthquake numbers along the profiles, excluding upper plate seismicity.

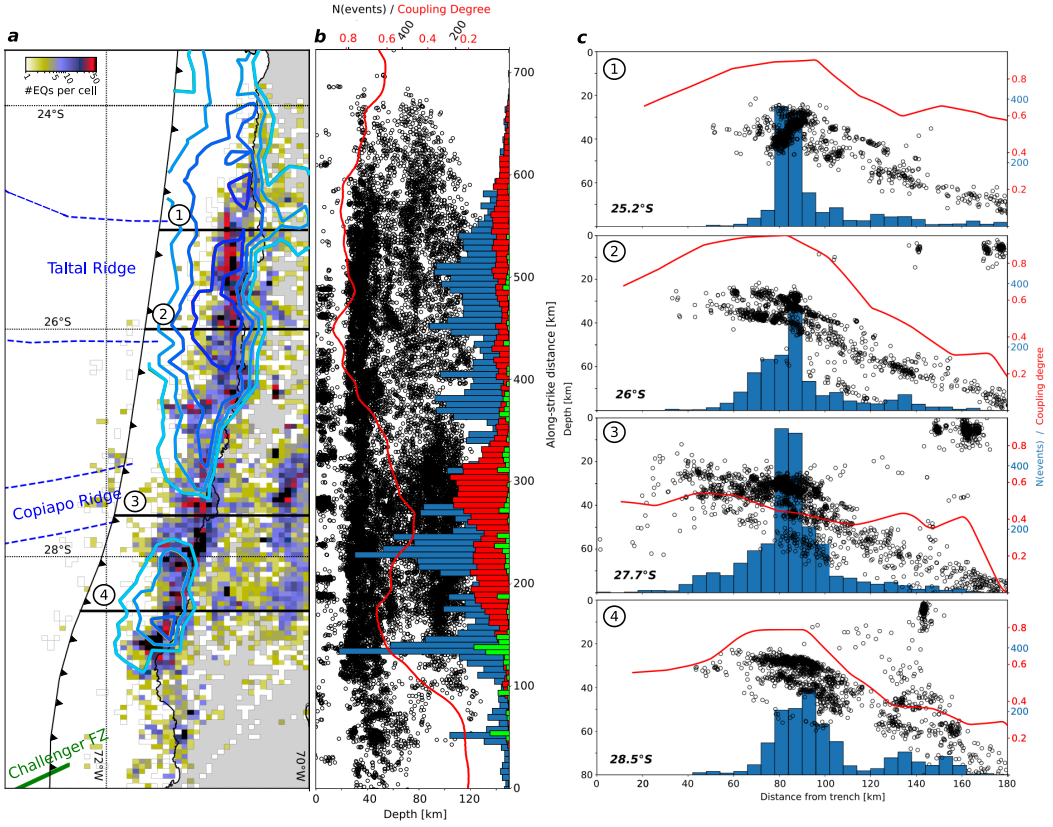

Figure 3. Correlating seismicity and interplate locking patterns. a) Map view plot of seismicity density, showing contours of mean interplate locking (0.6, 0.7, 0.8 and 0.9) as well as features on the downgoing oceanic plate. Black lines mark the locations of the W-E profiles shown in subfigure c). b) Projection of seismicity onto a single longitudinal plane. Histogram in blue represents the amount of seismicity in the vicinity of the plate interface (20-70 km depth), histogram in red the intermediate-depth seismicity (depth >70 km), and histogram in green the repeating earthquakes. Red line shows the average locking degree of the uppermost 40 km of the plate interface according to the locking model shown in Figure 1b. c) Narrow W-E profiles of seismicity (swath width ±0.2° around nominal latitude), showing event numbers in the depth range 20-70 km with the blue histograms. Red line represents the average locking degree in a swath of ±0.1° around the profile location.

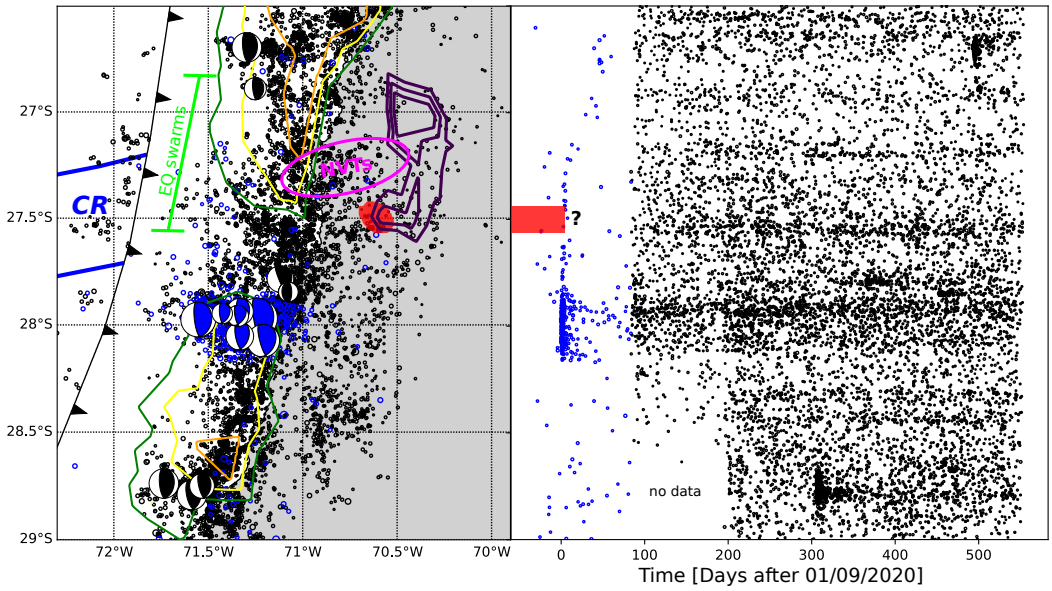

Figure 4. (left) Zoom-in to the weakly locked region ($\sim 27.5^{o}S$) onshore of the incoming Copiapó Ridge. Blue circles mark earthquakes between 01/08 and 23/11/2020, taken from the CSN catalog (Barrientos, 2018) and mostly showing the 2020 Atacama sequence (Klein et al., 2021). Black circles show earthquakes from our catalog, starting on 23/11/2020. Beachballs show lower-hemisphere projections of focal mechanisms for events with magnitude $\geq$4.8, taken from GEOFON. Purple contours mark the location of aseismic slip during the 2014 SSE (Klein, Duputel, et al., 2018), the red dot marks the approximate position of the 2020 SSE (Klein et al., 2023). The latitudinal range of earthquake swarms in 1973, 1979, 2006 and 2015 (Ojeda et al., 2023) is indicated by the green bracket, and the pink ellipse shows where non-volcanic tremor was identified in 2019 (Pastén-Araya et al., 2022). Green, yellow and orange lines mark locking degree contour lines of 0.6, 0.7 and 0.8. (right) Plot of earthquake latitudes against time, showing CSN catalog earthquakes in blue and our catalog in black. A horizontal stripe of increased seismicity is present at the latitude of the 2020 Atacama sequence. The red stripe marks the 2020 SSE.

Relation between oceanic plate structure, patterns of interplate locking and microseismicity in the 1922 Atacama Seismic Gap

Diego González-Vidal[1], Marcos Moreno[2], Christian Sippl[3], Juan Carlos Baez[4], Francisco Ortega-Culaciati[5], Dietrich Lange[6], Frederik Tilmann[7,12], Anne Socquet[8], Jan Bolte[9], Joaquin Hormazabal[5], Mickael Langlais[8], Catalina Morales-Yáñez[10], Daniel Melnick[1], Roberto Benavente[10,11], Rodolfo Araya[13]

[1]Department of Earth Sciences, University of Concepción, Barrio Universitario s/n, 4030000 Concepció, Chile

[2]Department of Engineering and Geotectonic, Pontifical Catholic University of Chile, Av. Vicuña Mackenna 4860, 8331150 Santiago, Chile

[3]Institute of Geophysics, Czech Academy of Sciences, Bocni II/1401, 14131 Prague, Czech Republic

[4]National Seismological Center, Faculty of Physical and Mathematical Sciences, University of Chile, Av. Beaucheff 1225, 8370583 Santiago, Chile

[5]Department of Geophysics, Faculty of Physical and Mathematical Sciences, University of Chile, Av. Blanco Encalada 2002, 8370449 Santiago, Chile

[6]GEOMAR Helmholtz Centre for Ocean Research Kiel, Wischhofstrasse 1-3, 24098 Kiel, Germany

[7]Department of Geophysics, Deutsches GeoForschungsZentrum GFZ, Wissenschaftpark "Albert Einstein", Telegrafenberg, 14473 Potsdam, Germany

[8]Univ. Grenoble Alpes, Univ. Savoie Mont Blanc, CNRS, IRD, Univ. Gustave Eiffel, ISTerre, 38000 Grenoble, France

[9]Department of Mathematics, University of Kiel, Christian-Albrechts-Platz 4, 24118 Kiel, Germany

[10]Department of Civil Engineering, Universidad Católica de la Santísima Concepción, 4030000 Concepción, Chile

[11]National Research Center for Integrated Natural Disaster Management (CIGIDEN), 8370583 Santiago, Chile.

[12]Institute of Geological Sciences, Freie Universität Berlin, Kaiserswerther Str. 16-18, 14195 Berlin, Germany

[13]Departamento de Ingeniería Matemática & CI2MA, Universidad de Concepción, 4030000 Concepción, Chile

Corresponding author: Marcos Moreno, `marcos.moreno@ing.puc.cl`

Key Points:

- Microseismicity catalog and map of interplate locking derived for the Atacama 1922 seismic gap in North-Central Chile
- Plate interface seismicity coincides with downdip edge of high coupling
- Seismo-geodetic signals due to the subduction of the Copiapó ridge are prominent but negligible for the subducting Taltal Ridge.

Abstract

We deployed a dense geodetic and seismological network in the Atacama seismic gap in Chile. We derive a microseismicity catalog of >30,000 events, time series from 70 GNSS stations, and apply a transdimensional Bayesian inversion to estimate interplate locking degree. We identify two highly locked regions of different sizes whose geometries appear to control seismicity patterns. Interface seismicity concentrates beneath the coastline just downdip of the highest locking. A region of lower interplate locking around 27.5°S coincides with higher seismicity levels, a high number of repeating earthquakes and events extending further towards the trench. Having shown numerous signs of aseismic deformation (slow-slip events and earthquake swarms), this area is situated where the Copiapó Ridge is subducted. While these findings suggest that the structure of the downgoing oceanic plate prescribes patterns of interplate locking and seismicity, we note that the Taltal Ridge further north lacks a similar signature.

Plain Language Summary

Deformation along plate boundaries can occur seismically (i.e. through earthquakes) as well as aseismically (i.e. slipping slowly), and it is important to understand where each of these modes is dominant. Along the Chilean subduction contact, North-Central Chile is the only place where aseismic deformation episodes have been observed so far. In order to study these processes in detail, we deployed and operated dense geodetic and seismological networks in this region. Analyzing the data collected by these networks, we find notable relationships between seismic and aseismic processes. Thousands of small earthquakes are found at the boundaries of locked regions, whereas no small earthquakes are found at their interior. Thus, implying such regions are mechanically coupled, i.e. currently accumulating elastic deformation energy that will one day be released during a large earthquake. Along the North-Central Chilean plate boundary, there is one region (around 27.5°S) that shows many signs of aseismic deformation. It is located where a chain of seamounts is being subducted, which is likely responsible for the different behavior of this segment.

1 Introduction

Relative motion along the subduction zone plate interface is partitioned between seismic and aseismic processes (e.g. Perfettini et al., 2010). The seismogenic zone of the

megathrust accumulates slip deficit and releases it seismically during large earthquakes (Lay et al., 2012). In contrast, the adjacent updip and downdip regions tend to yield aseismic slip to account for part or the totality of the plate convergence(e.g. Peng & Gomberg, 2010). The amount of convergence accommodated in large earthquakes versus continuous or transient creep is highly variable along strike in many subduction zones (Métois et al., 2016). Different forms of aseismic slip are observed along the plate interface. Slow-slip events (SSEs) are days-to-months long aseismic slip pulses that usually occur at the downdip end of the plate interface and are often accompanied by non-volcanic tremor (Schwartz & Rokosky, 2007). However, SSEs have also been observed in the shallowest part of the plate interface (e.g., Araki et al., 2017) or within the seismogenic zone. Aseismic slip transients have also been observed to precede large earthquakes (e.g., Ito et al., 2013; Radiguet et al., 2016; Socquet et al., 2017; Voss et al., 2018), as a mixture of slow deformation and foreshocks (Bedford et al., 2015). Finally, aseismic slip unrelated to large earthquakes has also been observed along weakly locked segments of the plate interface. Increased seismicity rates or swarm-like sequences have been found to occur in direct vicinity to – and likely triggered by – aseismic transients (Vallée et al., 2013; Hirose et al., 2014). Repeating earthquakes, recurring small events that repeatedly rupture the same fault area, are thought to be a direct consequence of ongoing aseismic deformation in their surroundings (Igarashi et al., 2003; Uchida & Bürgmann, 2019).

SSEs along the Chilean margin appear to be rare or at least more subtle. North-Central Chile is one of the few sites where transient slow-slip events have been observed independently from large megathrust earthquakes in Chile. A SSE event of ∼18 months duration with a maximum slip of about 50 cm was observed at the deepest part of the plate interface in 2014 and 2015 (Klein, Duputel, et al., 2018), and again in 2020 (Klein et al., 2023). Swarm-like seismicity sequences have been observed in 2006 and 2015 close to the town of Caldera, updip of the SSE's location (Holtkamp et al., 2011; Ojeda et al., 2023), as well as ∼50-100 km further south in 2020 (Klein et al., 2021). However, this segment of the margin has until recently only been sparsely instrumented, so that a first more comprehensive analysis of its seismicity has only recently been undertaken (Pastén-Araya et al., 2022). The Atacama region was struck by a great ($Mw \sim 8.5$) earthquake in 1922 and by a similar event in 1819 (Fig. 1a), thus being considered a mature seismic gap, at risk of breaking in a great subduction earthquake (e.g., Yáñez-Cuadra et al., 2022).

In this study we deployed a dense network of 85 seismic stations complementing 16 stations already installed in the region (see Text S3, Figures 1, S6). Additionally, we deployed 28 continuous GNSS stations to densify the already existing network composed by 42 GNSS sites (see Text S1, Figures S1-S3). We created a high-resolution microseismicity catalog comprising more than 30,000 events occurring for 15 months since November 2020. We compare such seismicity to interplate locking constrained by GNSS secular rates and estimated using a transdimensional Bayesian approach. In this scheme, the spatial resolution of the locking model is obtained in a data-driven manner without the need for a priori smoothing. From these we derive constraints on the interplay of seismic and aseismic processes in the region. In the following sections, we first describe the derivation of the locking model from geodetic observations, as well as the seismicity catalog from the measured seismic waveforms.

2 A transdimentional Bayesian estimation of interplate locking

We used data from a total of 70 GNSS stations located between 23°S and 32°S, where two new deployments provided a total of 28 new stations in addition to the backbone network of the National Seismological Center of Chile (Figure 1; Table S1). We processed the GNSS data using Bernese software to produce daily positional time series for the period between January 2018 and February 2023 (Dach et al., 2015; Teunissen & Montenbruck, 2017; "VMF Data Server", 2021). Then, we clean the time series and adjust a trajectory model to isolate the secular velocity for each station in the ITRF2014 system (Huang et al., 2012; Bevis & Brown, 2014; Báez et al., 2018; Köhne et al., 2023). We refer the reader to Supplementary Text S1 for further details.

Over the analyzed period, no transient motions are visible in the raw time series or in the residuals of the trajectory model. The estimated horizontal velocities show a gradual increase north of 29°S (Figure 1b). Between 29°S and 31°S, a decrease in the magnitude of the velocities is observed in the area of the 2015 (M_w8.3) Illapel earthquake rupture (Figure 1a). Vertical motion shows subsidence at coastal stations at 27.2°S and 29°S, which may be related to changes in the depth of the locked zone.

We use the resulting velocities to estimate the degree of locking along the subduction megathrust based on the backslip model (Savage, 1983). We compute Green's functions accounting for interseismic viscoelastic relaxation using a finite element model, fol-

lowing the approach and rheological properties used by Aagaard et al. (2013); Li et al. (2015). The interseismic deformation field in the forearc of northern and central Chile is affected not only by contraction induced by plate coupling, but also by continental deformation driven by the partitioning of tectonic deformation along continental structures (e.g. Yáñez-Cuadra et al., 2022). Thus, to estimate the degree of locking, it is necessary to subtract the contribution of continental deformation from the regional displacement field. Therefore, we corrected the velocities by subtracting the predicted regional continental deformation tensor estimated by Yáñez-Cuadra et al. (2022) from the estimated displacements (Figure 1b). To estimate the degree of locking, we perform a Bayesian transdimensional inversion (Green, 1995; Bodin & Sambridge, 2009; Sambridge, 2013) where samples from the posterior probability function of backslip are obtained using the reversible jump Markov chain Monte Carlo (rj-MCMC) method. In our approach, the spatial distribution of locking is discretized by Voronoi cells (Dettmer et al., 2014). The number and location of Voronoi cell centers are not fixed, but are allowed to vary according to a stochastic process. We impose constraints of positivity and maximum fault slip along the up-dip direction (up-dip slip ≥ 0 and smaller than convergence rate between the tectonic plates). We note that this methodology follows Bayesian parsimony, where the size of the Voronoi cells slip discretization is driven by the resolving capability of the data and the properties of the physical model. Therefore, in contrast to typical least-squares optimization approaches that need some prior spatial smoothing constraint to solve the inherently ill-posed slip inversion (e.g., Ortega-Culaciati et al., 2021), our approach does not require such a subjective smoothing of the slip distribution (see Supplementary Text S2).

Using the transdimensional approach, we obtain an ensemble of more than 1 million locking models. From the ensemble, we compute the mean locking distribution shown in Figure 1b. The model fit well the horizontal and vertical observations (Figure S2) and shows a pattern of locking degree that increases northward, similar to the gradient shown by the surface displacement field. Our results show high values of interplate locking in the offshore region, with mostly lower values (<0.6) beneath the onshore regions. The margin north of 27.5°S appears to be highly locked, with the highest values around 26°S. A second smaller, less prominent locking high is situated in the south of the study area, around 28-29°S. It is separated from the northern locking high by a narrow region with a significantly lower locking degree around 27.7°S, where no values exceeding 0.5 are found.

Locking degree is very low in the southernmost part of the study region, possibly due to contamination with postseismic signals from the 2015 (M_w8.3) Illapel earthquake.

3 Seismicity catalog

We analyzed data from 101 seismic stations located in the Atacama seismic gap (24.4°S – 30.3°S) that continuously recorded waveforms from November 2020 to July 2022 (Figure 1). Given the large amount of data, we used an automated earthquake detection and location workflow based on machine learning techniques for phase picking (EQTransformer; Mousavi et al., 2019, 2020; Münchmeyer et al., 2022; Woollam et al., 2022) and phase association (GaMMA; Zhu et al., 2022). We define events as having at least 7 P- and 4 S-phases resulting in a seismicity catalog that features 30,560 events, comprising 469,980 P-phases and 391,350 S-phases. We then successively relocated this catalog based on a 1D as well as a 2D velocity model that was derived from a subset of our data (Kissling et al., 1994; Thurber & Eberhart-Phillips, 1999; Havskov et al., 2020), before eventually applying hypoDD (Waldhauser & Ellsworth, 2000) to obtain double-difference relocations (see Text S3). We estimate average location errors to be <5 km inside the network, while they increase to 10-25 km outside the network toward the trench and volcanic arc. Local magnitudes range from 0.6 to 5.7 and we obtain an overall completeness magnitude of 1.6 (Figure S9).

The seismicity catalog is presented in Figure 2. The apparent decay of seismicity north of ∼24.5°S and south of ∼29.5°S is likely due to the lower detection capability plus shorter deployment times in such regions. A continuous band of high background seismicity beneath the coastline is the most prominent feature of the catalog. Events in this band, located ∼30-100 km from the trench, define two parallel planes with <10 km vertical separation in profile view (Figure 2b-e). While the upper plane likely corresponds to the deeper portion of the plate interface, its deepest (¿ ∼75 km) portion is located inside the downgoing slab and corresponds to the upper band of an occasionally visible double seismic zone (DSZ, e.g. Brudzinski et al., 2007; Sippl et al., 2018). Seismicity is scarce at the shallower part of the plate interface, extending closer to the trench along a total of four or five narrow features (Figure 2a), that also host significant concentrations of repeating earthquakes (see Text S4). Seawards of the trench, scattered events south of 26°S likely occurred in the outer rise region. Due to their location far outside the network, the depth of these events is very badly defined. East of the coastline, seis-

micity is largely found inside the downgoing slab, confined to the uppermost 25-30 km of the lithosphere. Most of this intraslab seismicity occurs at ∼50-120 km depth, between ∼150-300 km distance from the trench. The geometry and vigor of intraslab seismicity is highly variable along strike. In the north (Figure 2b), most seismicity occurs in the uppermost 10-15 km of the slab, whereas deeper levels (20-30 km below slab surface) are most active further south (Figure 2d,e). In profiles c and d of Figure 2, a clear DSZ with about 15 km separation between both bands is visible. The southward transition to the Pampean flat slab is accompanied by high seismicity levels deeper within the downgoing slab. We obtain 3,431 upper plate seismic events, defined as those located at <15 km depth and >5 km above the top of the subducted slab. Their occurrence rate is significantly increased during local daytime, suggesting a predominance of mining blast activity (Figure S10).

4 Discussion

4.1 Relation between microseismicity and interplate locking

Figure 3 summarizes the spatial relationship between interplate locking and the occurrence of microseismicity along the North-Central Chile margin. The highest concentration of microseismicity is found to occur just seawards and beneath the coastline (Figure 3a), with hypocentral depths between ∼25 and 40 km. This location roughly corresponds to the landward edge of the highly locked regions, indicating that most seismicity occurs where locking starts to decrease in the downdip direction (Figure 3c). In contrast, the shallow part of the megathrust is largely aseismic, and most seismicity that extends further towards the trench is confined to a weakly locked region between ∼27.5 and 28°S. When projected in the along-strike direction (Figure 3b), the highest seismicity concentrations and the largest number of repeating earthquakes (Uchida & Matsuzawa, 2013) can be found along the northern and southern terminations of the southern highly locked patch.

A very similar pattern of seismicity and interplate locking was found just south of the study region (Sippl et al., 2021), where it was interpreted as the signature of mature asperities on the megathrust. Accumulation of convergence over most of the seismic cycle creates a "halo" of high stresses around the downdip edge of highly locked regions (e.g. Moreno et al., 2018; Schurr et al., 2020). This "halo" may be the cause of the high

levels of background seismicity we observe on the deeper part of the plate interface. The weak locking and high seismicity we obtain around 27.7°S likely represents a segment of the megathrust that features more aseismic deformation. Weak locking in this location is a stable feature across all published locking maps of the area (Métois et al., 2016; Klein, Métois, et al., 2018; Yáñez-Cuadra et al., 2022), and numerous indicators for slow slip processes have been observed here (Section 4.2; Figure 4). The seismicity in the shallower part of the plate interface in this region is probably driven by such slow slip processes, which explains its absence in other, more highly locked regions of the megathrust.

The southern termination of the southern locked patch around 29°S features increased seismicity levels and elevated numbers of repeating earthquakes (Figure 2), similar to the region around 27.7°S. While the resolution of our catalog is very low south of ∼29°S, Sippl et al. (2021) shows an extended zone of increased shallow plate interface seismicity up to ∼30.5°S. This could hint the presence of aseismic processes related to the incoming Challenger Fracture Zone (Figures 1a and 3), which is thought to have prescribed the northern termination of the 2015 M_w 8.3 Illapel earthquake (e.g., Tilmann et al., 2016; Poli et al., 2017).

4.2 Seismic and aseismic signature of the Copiapó Ridge

Figure 4 summarizes observations of seismic and aseismic processes in the vicinity of the incoming Copiapó Ridge. A prominent offshore seismic swarm occurred in the region in 2006 (Holtkamp et al., 2011), and similar swarm occurrences have been reported for the years 1973, 1979 and 2015 (e.g., Ojeda et al., 2023). The 2014 SSE was situated further downdip but covered the same latitudinal range (Klein, Duputel, et al., 2018). A similar SSE was identified starting in March 2020, confined to the southern part of the 2014 SSE (Klein et al., 2023). Aseismic slip continued at least until September 2020, when the Atacama seismic sequence (see below) began to shadow the SSE signal. Non-volcanic tremor events observed in 2019 (Pastén-Araya et al., 2022) occurred directly updip of the 2014 SSE. In September 2020, only 2.5 months before the start of our catalog and GNSS observations, the Atacama seismic sequence occurred, featuring three major earthquakes of M>6. In addition, unusually large amounts of aseismic slip, equivalent to M_w 6.8, occurred within the weakly coupled patch between the mainshock of the Atacama seismic sequence and the southern edge of the 2014 SSE (Klein et al., 2021).

This sequence was situated along the southern edge of our inferences of weak locking, whereas all previously mentioned observations of earthquake swarms, SSEs and NVTs were situated 50-100 km further north (Figure 4). We found continued elevated background seismicity rates throughout the studied time interval in the latitudinal range of the 2020 Atacama sequence, accompanied by some repeating earthquakes (Figure 2).

Taken together, all these observations highlight the complex interplay of seismic and aseismic processes in the direct vicinity of the subduction of the Copiapó Ridge. It has previously been shown that elevated roughness on the downgoing plate leads to reduced interplate coupling (Wang & Bilek, 2014), as well as the formation of weakly coupled, creeping segments that may act as "barriers" to large earthquakes due to the lack of stress accumulation. Subducting ridges have also been shown to feature enhanced hydration of the downgoing plate, which can further reduce interplate coupling through the release of fluids and the subsequent increase of pore fluid pressure on the plate interface (e.g. Moreno et al., 2014). While these observations suggest that the region around 27.7°S represents a weakly locked "barrier" that may hinder the propagation of large megathrust earthquakes, the two last major earthquakes in 1922 and 1819 have both ruptured across it (Figure 1a). North of 26°S, the Taltal Ridge impinges onto the North-Central Chilean margin. Although its offshore bathymetric expression is similar to the Copiapó Ridge (Figure 1), we do not retrieve a region of lower interplate locking degree or elevated seismicity in this region (Figures 1 and 3). Whether this implies that the Taltal Ridge has only recently started to be subducted, or whether it possesses properties that clearly distinguish it from the Copiapó Ridge, is currently unclear.

4.3 Intraslab seismicity

Here we only provide a brief general overview of intraslab seismicity, with a more detailed analysis delegated to a future study. Our catalog shows Nazca plate intraslab seismicity occurring at depths ranging 35-∼120 km. A DSZ can be recognized, with its upper seismicity band most vigorously active directly beneath where most plate interface seismicity occurs (Figure 2c). The lower band of the DSZ, located ∼15 km below the upper band, within the downgoing slab, shows only weak activity at depths shallower than 80 km. At larger depths, seismicity in deeper levels of the slab intensifies. Thus, being harder to distinguish the two bands of the DSZ, as seismicity fills the gap between the two zones, in a similar manner as independent observations in Northern Chile (e.g.

Sippl et al., 2018). Most of this deeper intraslab seismicity is concentrated south of 27°S, with a clear maximum around 27.4°S. Intraslab earthquakes at intermediate depths are thought to be related to dehydration processes in the downgoing oceanic lithosphere (e.g. Hacker et al., 2003; Zhan, 2020). It is widely assumed that the loci and rate of seismicity in the slab represent the distribution of fluid release at depth. The concentration of deeper seismicity around 27.4°S may be the signature of increased hydration of the downgoing Copiapó Ridge. Streaks of increased intermediate-depth seismicity have been previously shown along the trace of downgoing ocean features along the Chilean margin (e.g. Kirby et al., 1996; Geersen et al., 2022). We could hypothesize there is a direct causal link between the different signatures of the Copiapó Ridge on the plate interface (low locking degree and seismicity) and within the slab (increased seismicity), through fluid processes, for instance. Alternatively, both behaviors may be independent consequences of ridge subduction. Discriminating between these hypotheses is beyond the scope of this contribution. We note that the signature of the Taltal Ridge further north is again less clearly visible, if present at all.

5 Conclusions

We combine novel highly resolved seismological and geodetic observations and model these using frontier techniques. Our results identify a number of distinct seismic and aseismic patterns that appear to be mainly influenced by the structure of the downgoing Nazca Plate. Our inferred locking distribution suggests that the Atacama seismic gap consists of two highly coupled regions of different sizes, separated by a creeping corridor with higher background seismicity. The geometry of these two "asperities" appears to control seismicity patterns. While the highly locked shallow part of the plate interface presents scarce seismicity, the downdip limit of interplate locking is marked by a band of background seismicity located beneath the coastline. Interplate locking decreases significantly around 27.7°S, where seismicity reaches shallower depths and numerous indicators for ongoing aseismic slip processes have been observed. The subduction of the Copiapó Ridge at this latitude creates a clear signature along the megathrust and at deeper depths inside the downgoing slab, both as a consequence of bathymetric roughness and/or increased (de)hydration.

Acknowledgments

Field work and instrumentation were funded by the ANILLO ACT192169 grant, ERC Deep-Trigger 865963 project and GFZ-Potsdam. M. M., D. G.V.,J.C. B., F. O.C., J.H., C.M.Y., D.M., R.B. acknowledge support from the ANILLO Precursor grant ACT192169. M.M., D.M. acknowledges FONDECYT 1221507 and the Millennium Nucleus "The Seismic Cycle Along Subduction Zones" grant NC160025. C.S. received funding from the European Research Council (ERC) through the Horizon 2020 program (ERC Starting Grant MILESTONE; StG2020-947856). C. M.Y. acknowledges support from FONDECYT 3220307. A.S. received funding from the European Research Council (ERC) CoG 865963 DEEP-trigger. Finally, we thank the GFZ Potsdam GIPP, B. Heit and the French national pool of portable seismic instruments SISMOB-RESIF (INSU-CNRS) for providing the seismological instruments and related metadata used in this study. Powered@NLHPC: This research was partially supported by the supercomputing infrastructure of the NLHPC (ECM-02).

Author Contribution

Experiment design: F. Tilmann, M. Moreno, J.C. Baez, F. Ortega-Culaciati, A. Socquet, M. Langlais, D. Melnick

Funding acquisition: F. Tilmann, M. Moreno, F. Ortega-Culaciati, A. Socquet, D. Melnick.

Methodology: D. González-Vidal, C. Sippl, M. Moreno, D. Lange, J.C. Baez, F. Ortega-Culaciati.

Software: J. Bolte, M. Moreno, J.C. Baez, F. Ortega-Culaciati, C. Sippl, D. Lange.

Analysis of seismic data: D. González-Vidal, C. Sippl, D. Lange, C. Morales.

Analysis of GNSS data: M. Moreno, J.C. Baez, F. Ortega-Culaciati.

Figures: D. González-Vidal, C. Sippl, M. Moreno.

Writing - original draft: C. Sippl, M. Moreno, D. González-Vidal, J.C. Baez.

Writing - review and editing: everyone

Data Availability

The seismic waveforms we used in this paper to compile the earthquake catalog was retrieved from the GEOFON data centre of the GFZ German Research Centre for Geosciences and IRIS Web, and come from the networks Y6 (Tilmann et al., 2021), XZ (Socquet

et al., 2025), CX (GFZ & CNRS-INSU, 2006), C1 (Universidad de Chile, 2013), C (https://www.fdsn.org/network and IU (Albuquerque Seismological Laboratory/USGS (ASL), 2014). XZ data are archived at the EPOS-FRANCE RESIF data center (https://seismology.resif.fr/fr/reseaux/#/XZ_2020) and will be opened at the end of the project (2026). Moment tensors used in Figure 4 were retrieved from the GEOFON program of the GFZ German Research Centre for Geosciences (https://geofon.gfz-potsdam.de/eqinfo/). The earthquake catalog, GNSS time series and locking model presented in this article will be available as a data publication at the GFZ Data Center at https://nextcloud.gfz-potsdam.de/s/oGAbANpe2jQiBzd (temporary link; the dataset will be archived at GFZ data services and a DOI issued for it after taking into account reviewer comments).

References

Aagaard, B. T., Knepley, M. G., & Williams, C. A. (2013). A domain decomposition approach to implementing fault slip in finite-element models of quasi-static and dynamic crustal deformation. *Journal of Geophysical Research: Solid Earth*, *118*(6), 3059-3079. Retrieved from `https://agupubs.onlinelibrary.wiley.com/doi/abs/10.1002/jgrb.50217` doi: 10.1002/jgrb.50217

Albuquerque Seismological Laboratory/USGS (ASL). (2014). *Global Seismograph Network (GSN - IRIS/USGS) [Dataset].* Federation of Digital Seismograph Networks. doi: https://doi.org/10.7914/SN/IU

Araki, E., Saffer, D., Kopf, A. J., Wallace, L., Kimura, T., Machida, Y., ... Davis, E. (2017). Recurring and triggered slow-slip events near the trench at the Nankai Trough subduction megathrust. *Science*, *356*(6343), 1157–1160. doi: 10.1126/science.aan3120

Barrientos, S. (2018). The Seismic Network of Chile. *Seismological Research Letters*, *89*(2A), 467–474. doi: 10.1785/0220160195

Bedford, J., Moreno, M., Schurr, B., Bartsch, M., & Oncken, O. (2015). Investigating the final seismic swarm before the iquique-pisagua 2014 mw 8.1 by comparison of continuous gps and seismic foreshock data. *Geophysical Research Letters*, *42*(10), 3820-3828. doi: https://doi.org/10.1002/2015GL063953

Bevis, M., & Brown, A. (2014). Trajectory models and reference frames for crustal motion geodesy. *Journal of Geodesy*, *88*, 283–311. doi: 10.1007/s00190-013

-0685-5

Bodin, T., & Sambridge, M. (2009). Seismic tomography with the reversible jump algorithm. *Geophysical Journal International*, *178*, 1411-1436.

Brudzinski, M. R., Thurber, C. H., Hacker, B. R., & Engdahl, E. R. (2007). Global prevalence of double benioff zones. *Science*, *316*(5830), 1472–1474. doi: 10.1126/science.1139204

Báez, J. C., Leyton, F., Troncoso, C., del Campo, F., Bevis, M., Vigny, C., ... Blume, F. (2018). The Chilean GNSS Network: Current Status and Progress toward Early Warning Applications. *Seismological Research Letters*, *89*(4), 1546-1554. doi: 10.1785/0220180011

Dach, R., Lutz, S., Walser, P., & Fridez, P. e. (2015). Bernese GNSS Software Version 5.2. In *University of Bern, Bern Open Publishing.* doi: 10.7892/boris.72297

Dettmer, J., Benavente, R., Cummins, P. R., & Sambridge, M. (2014). Trans-dimensional finite-fault inversion. *Geophysical Journal International*, *199*(2), 735-751. doi: 10.1093/gji/ggu280

Geersen, J., Sippl, C., & Harmon, N. (2022). Impact of bending-related faulting and oceanic-plate topography on slab hydration and intermediate-depth seismicity. *Geosphere*, *18*(2), 562–584. doi: https://doi.org/10.1130/GES02367.1

GFZ, & CNRS-INSU. (2006). *IPOC Seismic Network: Integrated Plate boundary Observatory Chile - IPOC.* GFZ Data Services. doi: 10.14470/PK615318

Green, P. J. (1995). Reversible jump Markov chain Monte Carlo computation and Bayesian model determination. *Biometrika*, *82*, 711-732.

Hacker, B. R., Peacock, S. M., Abers, G. A., & Holloway, S. D. (2003). Subduction factory 2. Are intermediate-depth earthquakes in subducting slabs linked to metamorphic dehydration reactions? *Journal of Geophysical Research*, *108*(B1). doi: 10.1029/2001JB001129

Havskov, J., Voss, P. H., & Ottemöller, L. (2020, 03). Seismological Observatory Software: 30 Yr of SEISAN. *Seismological Research Letters*, *91*(3), 1846-1852. doi: 10.1785/0220190313

Hayes, G. P., Moore, G., Portner, D. E., Hearne, M., Flamme, H., Furtney, M., & Smoczyk, G. M. (2018). Slab2, a comprehensive subduction zone geometry model. *Science*, *362*(6410), 58–61. doi: 10.1126/science.aat4723

Hirose, H., Matsuzawa, T., Kimura, T., & Kimura, H. (2014). The Boso slow slip events in 2007 and 2011 as a driving process for the accompanying earthquake swarm. *Geophysical Research Letters*, *41*(8), 2778–2785. doi: 10.1002/2014GL059791

Holtkamp, S. G., Pritchard, M. E., & Lohman, R. B. (2011). Earthquake swarms in South America. *Geophysical Journal International*, *187*(1), 128–146.

Huang, D., Dai, W., & Luo, F. (2012, 10). Ica spatiotemporal filtering method and its application in gps deformation monitoring. *Applied Mechanics and Materials*, *204-208*, 2806-2812. doi: 10.4028/www.scientific.net/AMM.204-208.2806

Igarashi, T., Matsuzawa, T., & Hasegawa, A. (2003). Repeating earthquakes and interplate aseismic slip in the northeastern Japan subduction zone. *Journal of Geophysical Research: Solid Earth*, *108*(B5), 1–9. doi: 10.1029/2002jb001920

Ito, Y., Hino, R., Kido, M., Fujimoto, H., Osada, Y., Inazu, D., ... Ashi, J. (2013). Episodic slow slip events in the japan subduction zone before the 2011 tohoku-oki earthquake. *Tectonophysics*, *600*, 14-26. doi: https://doi.org/10.1016/j.tecto.2012.08.022

Kirby, S., Engdahl, E. R., & Denlinger, R. (1996). Intermediate-depth intraslab earthquakes and arc volcanism as physical expressions of crustal and uppermost mantle metamorphism in subducting slabs. *Geophysical Monograph Series*, *96*, 195–214. doi: 10.1029/GM096p0195

Kissling, E., Ellsworth, W. L., Eberhart-Phillips, D., & Kradolfer, U. (1994). Initial reference models in local earthquake tomography. *Journal of Geophysical Research*, *99*(B10), 19,635–19,646.

Klein, E., Duputel, Z., Zigone, D., Vigny, C., Boy, J. P., Doubre, C., & Meneses, G. (2018). Deep Transient Slow Slip Detected by Survey GPS in the Region of Atacama, Chile. *Geophysical Research Letters*, *45*(22), 12,263–12,273. doi: 10.1029/2018GL080613

Klein, E., Métois, M., Meneses, G., Vigny, C., & Delorme, A. (2018). Bridging the gap between North and Central Chile: Insight from new GPS data on coupling complexities and the Andean sliver motion. *Geophysical Journal International*, *213*(3), 1924–1933. doi: 10.1093/gji/ggy094

Klein, E., Potin, B., Pasten-Araya, F., Tissandier, R., Azua, K., Duputel, Z., ... Vigny, C. (2021). Interplay of seismic and a-seismic deformation during the

2020 sequence of Atacama , Chile. *Earth and Planetary Science Letters*, *570*, 117081. doi: 10.1016/j.epsl.2021.117081

Klein, E., Vigny, C., Duputel, Z., Zigone, D., Rivera, L., Ruiz, S., & Potin, B. (2023). Return of the Atacama deep Slow Slip Event: The 5-year recurrence confirmed by continuous GPS. *Physics of the Earth and Planetary Interiors*, *334*, 106970. doi: 10.1016/j.pepi.2022.106970

Köhne, T., Riel, B., & Simons, M. (2023). Decomposition and inference of sources through spatiotemporal analysis of network signals: The disstans python package. *Computers & Geosciences*, *170*, 105247. doi: https://doi.org/10.1016/j.cageo.2022.105247

Lay, T., Kanamori, H., Ammon, C. J., Koper, K. D., Hutko, A. R., Ye, L., ... Rushing, T. M. (2012). Depth-varying rupture properties of subduction zone megathrust faults. *Journal of Geophysical Research*, *117*(4), B04311. doi: 10.1029/2011JB009133

Li, S., Moreno, M., Bedford, J., Rosenau, M., & Oncken, O. (2015). Revisiting viscoelastic effects on interseismic deformation and locking degree: A case study of the peru-north chile subduction zone. *Journal of Geophysical Research: Solid Earth*, *120*(6), 4522-4538. doi: https://doi.org/10.1002/2015JB011903

Métois, M., Vigny, C., & Socquet, A. (2016). Interseismic Coupling, Megathrust Earthquakes and Seismic Swarms Along the Chilean Subduction Zone (38°–18°S). *Pure and Applied Geophysics*, *173*(5), 1431–1449. doi: 10.1007/s00024-016-1280-5

Moreno, M., Haberland, C., Oncken, O., Rietbrock, A., Angiboust, S., & Heidbach, O. (2014). Locking of the Chile subduction zone controlled by fluid pressure before the 2010 earthquake. *Nature Geoscience*, *7*(4), 292–296. doi: 10.1038/ngeo2102

Moreno, M., Li, S., Melnick, D., Bedford, J., Baez, J. C., Motagh, M., ... Oncken, O. (2018). Chilean megathrust earthquake recurrence linked to frictional contrast at depth. *Nature Geoscience*, *11*(4), 285–290. doi: 10.1038/s41561-018-0089-5

Mousavi, S. M., Ellsworth, W. L., Zhu, W., Chuang, L. Y., & Beroza, G. C. (2020). Earthquake transformer—an attentive deep-learning model for simultaneous earthquake detection and phase picking. *Nature Communications*, *11*. doi:

10.1038/s41467-020-17591-w

Mousavi, S. M., Sheng, Y., Zhu, W., & Beroza, G. C. (2019). STanford EArthquake Dataset (STEAD): A Global Data Set of Seismic Signals for AI. *IEEE Access*, *7*, 179464–179476. Retrieved from `http://dx.doi.org/10.1109/ACCESS.2019.2947848` doi: 10.1109/access.2019.2947848

Münchmeyer, J., Woollam, J., Rietbrock, A., Tilmann, F., Lange, D., Bornstein, T., ... Soto, H. (2022). Which picker fits my data? a quantitative evaluation of deep learning based seismic pickers. *Journal of Geophysical Research: Solid Earth*, *127*. doi: 10.1029/2021JB023499

Ojeda, J., Morales-Yáñez, C., Ducret, G., Ruiz, S., Grandin, R., Doin, M.-P., ... Nocquet, J.-M. (2023). Seismic and aseismic slip during the 2006 Copiapo swarm in North-Central Chile. *Journal of South American Earth Sciences*, 104198. doi: 10.1016/j.jsames.2023.104198

Ortega-Culaciati, F., Simons, M., Ruiz, J., Rivera, L., & Díaz-Salazar, N. (2021). An epic tikhonov regularization: Application to quasi-static fault slip inversion. *Journal of Geophysical Research: Solid Earth*, *126*(7), e2020JB021141. doi: 10.1029/2020JB021141

Pastén-Araya, F., Potin, B., Azúa, K., Sáez, M., Aden-Antoniów, F., Ruiz, S., ... Duputel, Z. (2022). Along-Dip Segmentation of the Slip Behavior and Rheology of the Copiapó Ridge Subducted in North-Central Chile. *Geophysical Research Letters*(49), e2021GL095471. doi: 10.1029/2021gl095471

Peng, Z., & Gomberg, J. (2010). An integrated perspective of the continuum between earthquakes and slow-slip phenomena. *Nature Geoscience*, *3*(9), 599–607. doi: 10.1038/ngeo940

Perfettini, H., Avouac, J.-P., Tavera, H., Kositsky, A., Nocquet, J. M., Bondoux, F., ... Soler, P. (2010). Seismic and aseismic slip on the Central Peru megathrust. *Nature*, *465*(7294), 78–81. doi: 10.1038/nature09062

Poli, P., Jeria, A. M., & Ruiz, S. (2017). The Mw 8.3 lllapel earthquake (Chile): Preseismic and postseismic activity associated with hydrated slab structures. *Geology*, *45*(3), 247–250. doi: 10.1130/G38522.1

Radiguet, M., Perfettini, H., Cotte, N., Gualandi, A., Valette, B., Kostoglodov, V., ... Campillo, M. (2016). Triggering of the 2014 m w 7.3 papanoa earthquake by a slow slip event in guerrero, mexico. *Nature Geoscience*, *9*(11), 829–833.

Sambridge, M. (2013, 10). A Parallel Tempering algorithm for probabilistic sampling and multimodal optimization. *Geophysical Journal International*, *196*(1), 357-374. doi: 10.1093/gji/ggt342

Savage, J. C. (1983). A dislocation model of strain accumulation and release at a subduction zone. *Journal of Geophysical Research: Solid Earth*, *88*(B6), 4984-4996. doi: https://doi.org/10.1029/JB088iB06p04984

Schurr, B., Moreno, M., Tréhu, A. M., Bedford, J., Kummerow, J., Li, S., & Oncken, O. (2020). Forming a Mogi Doughnut in the Years Prior to and Immediately Before the 2014 M8.1 Iquique, Northern Chile, Earthquake. *Geophysical Research Letters*, *47*(16). doi: 10.1029/2020GL088351

Schwartz, S. Y., & Rokosky, J. M. (2007). Slow slip events and seismic tremor at circum-pacific subduction zones. *Reviews of Geophysics*, *45*(3), RG3004. doi: 10.1029/2006RG000208

Sippl, C., Moreno, M., & Benavente, R. (2021). Microseismicity appears to outline highly coupled regions on the Central Chile megathrust. *Journal of Geophysical Research: Solid Earth*, *126*, e2021JB022252. doi: 10.1029/2021jb022252

Sippl, C., Schurr, B., Asch, G., & Kummerow, J. (2018). Seismicity structure of the northern chile forearc from >100,000 double-difference relocated hypocenters. *Journal of Geophysical Research: Solid Earth*, *123*, 4063-4087. doi: 10.1002/2017JB015384

Socquet, A., Baez, J. C., Moreno, M., Langlais, M., & DEEP-Trigger Team and Geophysics Technical Service at ISTerre and RESIF. (2025). *DEEP-TRIGGER temporary experiment in the subduction zone Peru/Chile, Chile.* RESIF - Réseau Sismologique et géodésique Français. doi: 10.15778/RESIF.XZ2020

Socquet, A., Valdes, J. P., Jara, J., Cotton, F., Walpersdorf, A., Cotte, N., ... Norabuena, E. (2017). An 8 month slow slip event triggers progressive nucleation of the 2014 Chile megathrust. *Geophysical Research Letters*, *44*(9), 4046–4053. doi: 10.1002/2017GL073023

Tassara, A., & Echaurren, A. (2012). Anatomy of the Andean subduction zone: Three-dimensional density model upgraded and compared against global-scale models. *Geophysical Journal International*, *189*, 161–168.

Teunissen, P. J., & Montenbruck, O. (2017). *Springer Handbook of Global Navigation Satellite Systems.* Springer Cham. doi: https://doi.org/10.1007/978-3-319

-42928-1

Thurber, C. H., & Eberhart-Phillips, D. (1999). Local earthquake tomography with flexible gridding. *Computers and Geosciences*, *25*(7), 809–818. doi: 10.1016/S0098-3004(99)00007-2

Tilmann, F., Heit, B., Moreno, M., & González-Vidal, D. (2021). *Anillo.* GFZ Data Services. doi: 10.14470/L17575324477

Tilmann, F., Zhang, Y., Moreno, M., Saul, J., Eckelmann, F., Palo, M., ... Dahm, T. (2016). The 2015 Illapel earthquake, central Chile: a type case for a characteristic earthquake ? *Geophysical Research Letters*, *43*, 574–583. doi: 10.1002/2015GL066963

Uchida, N., & Bürgmann, R. (2019). Repeating Earthquakes. *Annual Review of Earth and Planetary Sciences*, *47*(1), 305–332. doi: 10.1146/annurev-earth-053018-060119

Uchida, N., & Matsuzawa, T. (2013). Pre- and postseismic slow slip surrounding the 2011 Tohoku-oki earthquake rupture. *Earth and Planetary Science Letters*, *374*, 81-91. doi: 10.1016/j.epsl.2013.05.021

Universidad de Chile. (2013). *Red Sismologica Nacional. International Federation of Digital Seismograph Networks.* doi: https://doi.org/10.7914/SN/C1

Vallée, M., Nocquet, J. M., Battaglia, J., Font, Y., Segovia, M., Régnier, M., ... Chlieh, M. (2013). Intense interface seismicity triggered by a shallow slow slip event in the Central Ecuador subduction zone. *Journal of Geophysical Research: Solid Earth*, *118*(6), 2965–2981. doi: 10.1002/jgrb.50216

VMF Data Server. (2021). In *re3data.org: Vmf data server; editing status 2021-08-24; re3data.org - registry of research data repositories.* doi: http://doi.org/10.17616/R3RD2H

Voss, N., Dixon, T. H., Liu, Z., Malservisi, R., Protti, M., & Schwartz, S. (2018). Do slow slip events trigger large and great megathrust earthquakes? *Science advances*, *4*(10), eaat8472.

Waldhauser, F., & Ellsworth, W. L. (2000). A Double-difference Earthquake location algorithm: Method and application to the Northern Hayward Fault, California. *Bulletin of the Seismological Society of America*, *90*(6), 1353–1368. doi: 10.1785/0120000006

Wang, K., & Bilek, S. L. (2014). Invited review paper: Fault creep caused by sub-

duction of rough seafloor relief. *Tectonophysics*, *610*, 1–24. doi: 10.1016/j.tecto .2013.11.024

Woollam, J., Münchmeyer, J., Tilmann, F., Rietbrock, A., Lange, D., Bornstein, T., ... Soto, H. (2022). SeisBench—A Toolbox for Machine Learning in Seismology. *Seismological Research Letters*, *93*(3), 1695-1709. doi: 10.1785/0220210324

Yáñez-Cuadra, V., Ortega-Culaciati, F., Moreno, M., Tassara, A., Krumm-Nualart, N., Ruiz, J., ... Benavente, R. (2022). Interplate Coupling and Seismic Potential in the Atacama Seismic Gap (Chile): Dismissing a Rigid Andean Sliver. *Geophysical Research Letters*, 1–26. doi: 10.1029/2022gl098257

Zhan, Z. (2020). Mechanisms and Implications of Deep Earthquakes. *Annual Review of Earth and Planetary Sciences*, *48*, 147–174. doi: 10.1146/annurev -earth-053018-060314

Zhu, W., McBrearty, I. W., Mousavi, S. M., Ellsworth, W. L., & Beroza, G. C. (2022). Earthquake phase association using a bayesian gaussian mixture model. *Journal of Geophysical Research: Solid Earth*, *127*(5), e2021JB023249. (e2021JB023249 2021JB023249) doi: https://doi.org/10.1029/2021JB023249

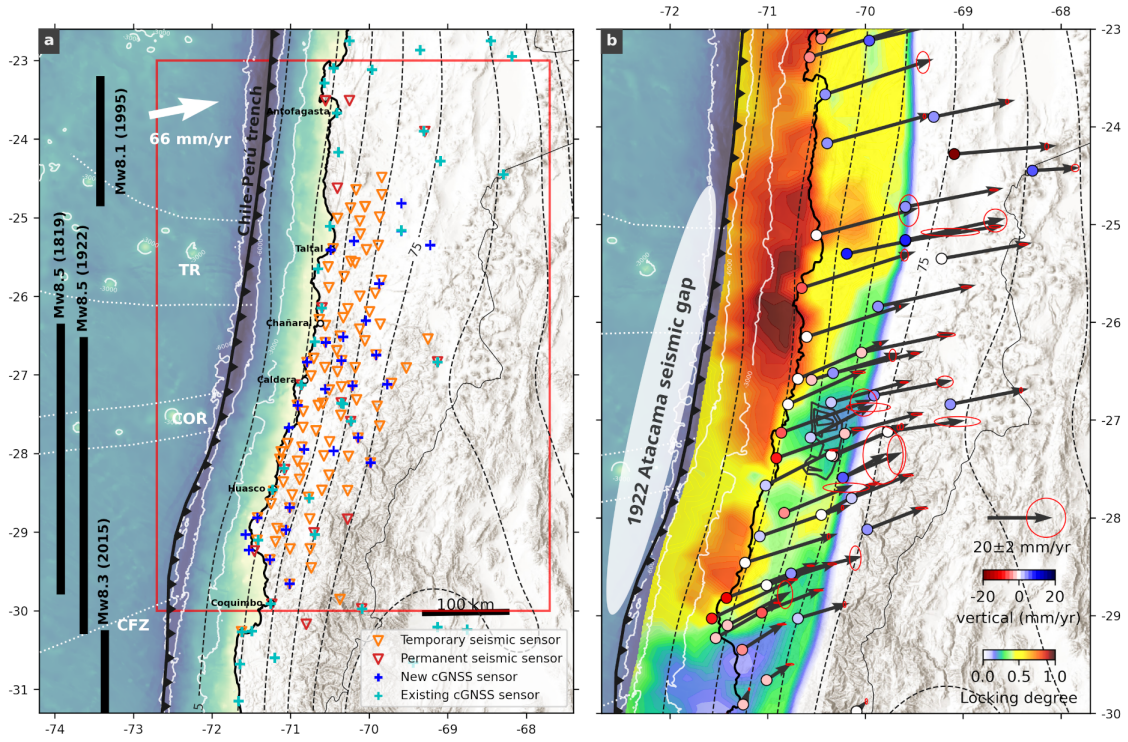

Figure 1. (a) Map view showing the distribution of existing and new GNSS and seismic networks in North-central Chile. The slab surface after model slab2 (Hayes et al., 2018) is shown with dashed black contour lines at 15 km intervals, the black barbed line marks the Chile-Perú trench and the white dotted outlines show prominent seafloor features (CFZ - Challenger Fracture Zone; COR - Copiapó Ridge; TR - Taltal Ridge). Rupture extents of historical megathrust earthquakes (M>8) are shown on the left. The red rectangle shows the extent of subfigure b). (b) Horizontal (vectors) and vertical (point coloring) velocities and uncertainties (red ellipses) of GNSS stations used in this study, shown together with the derived mean interplate locking model. The extent of the 1922 Atacama seismic gap is shown by the white ellipse on the left.

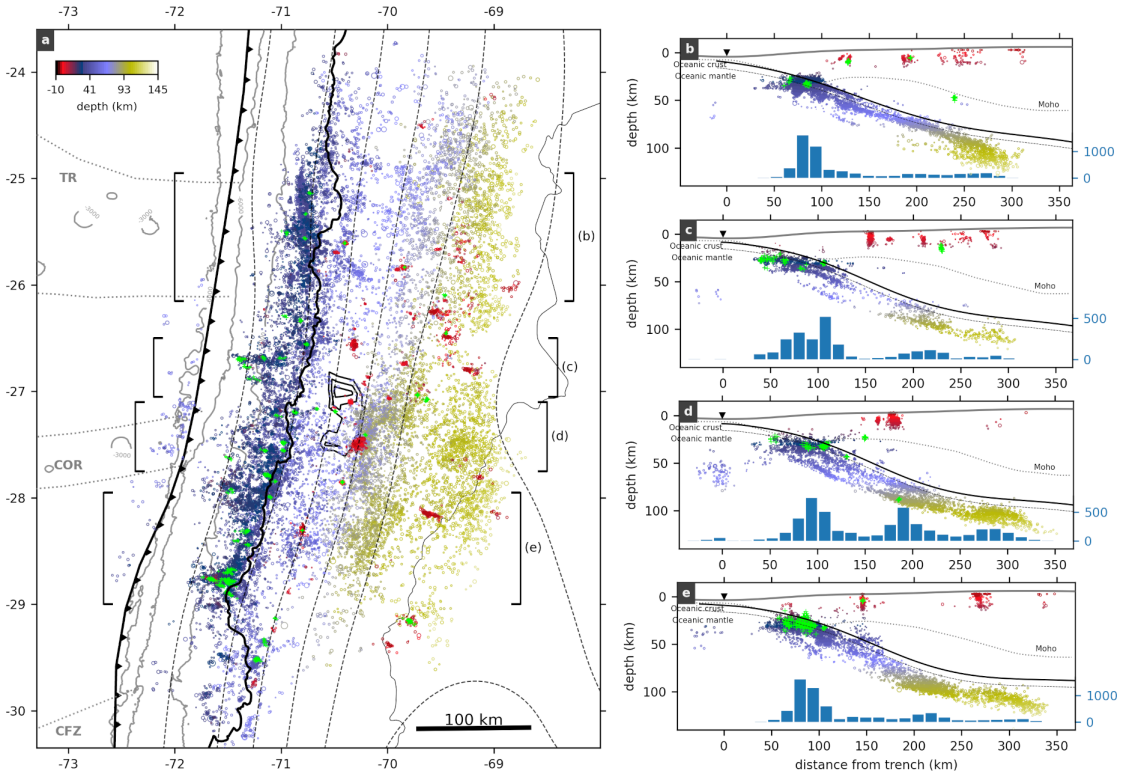

Figure 2. Map view (a) and profile projections (b-e) of the 30,560 hypocenters in the seismicity catalog, color-coded by depth. Families of repeaters are shown by green plus markers. The locations and swath widths of the profile projections are indicated by the black brackets in subfigure a). The black barbed line in the map view plot marks the location of the trench, the dotted pale grey lines show prominent seafloor features. The slab2 slab surface (Hayes et al., 2018) is shown with dashed contour lines in a) and with solid lines in the profile plots. The dashed black line in the profiles shows the inferred oceanic Moho located 7km below the slab2 surface. The dotted thin line shows the continental Moho from Tassara and Echaurren (2012). The position of the trench is marked by black inverted triangles. The blue histograms show earthquake numbers along the profiles, excluding upper plate seismicity.

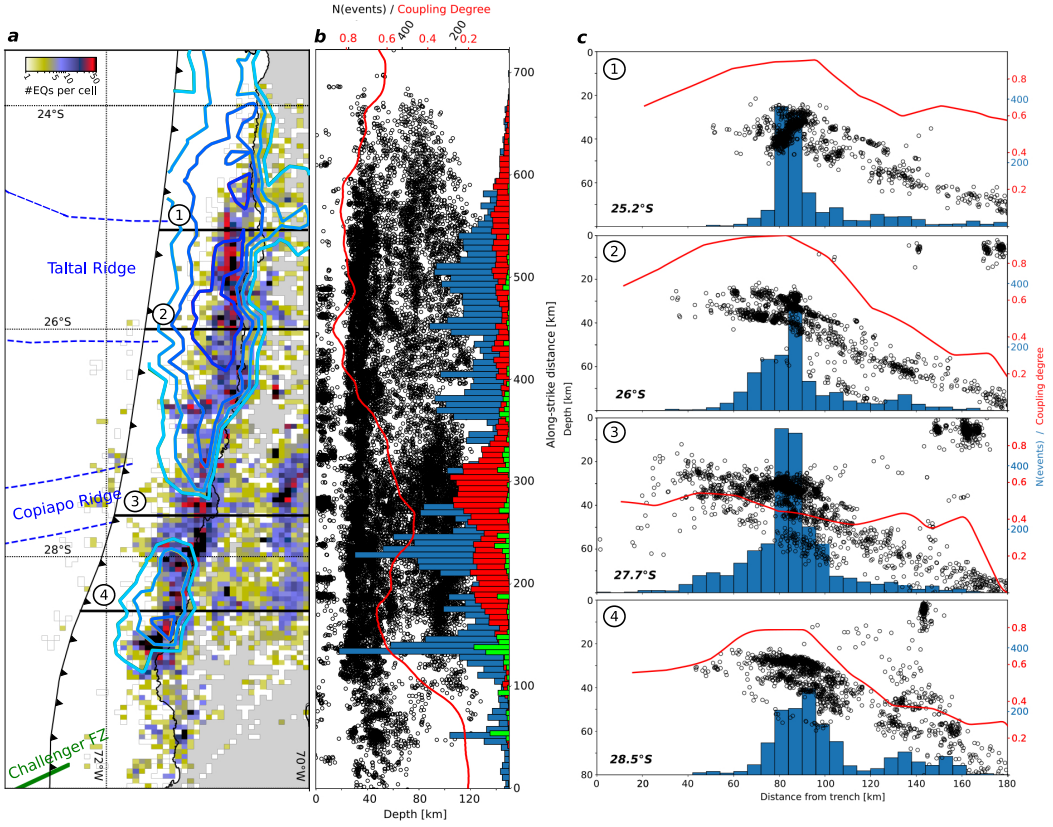

Figure 3. Correlating seismicity and interplate locking patterns. a) Map view plot of seismicity density, showing contours of mean interplate locking (0.6, 0.7, 0.8 and 0.9) as well as features on the downgoing oceanic plate. Black lines mark the locations of the W-E profiles shown in subfigure c). b) Projection of seismicity onto a single longitudinal plane. Histogram in blue represents the amount of seismicity in the vicinity of the plate interface (20-70 km depth), histogram in red the intermediate-depth seismicity (depth >70 km), and histogram in green the repeating earthquakes. Red line shows the average locking degree of the uppermost 40 km of the plate interface according to the locking model shown in Figure 1b. c) Narrow W-E profiles of seismicity (swath width ±0.2° around nominal latitude), showing event numbers in the depth range 20-70 km with the blue histograms. Red line represents the average locking degree in a swath of ±0.1° around the profile location.

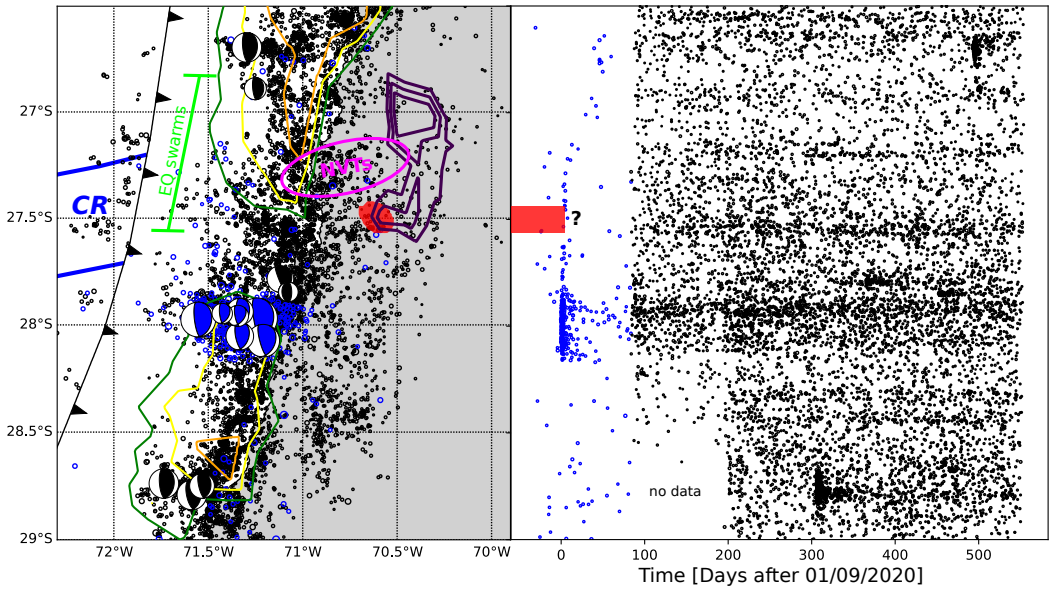

Figure 4. (left) Zoom-in to the weakly locked region ($\sim 27.5^{o}S$) onshore of the incoming Copiapó Ridge. Blue circles mark earthquakes between 01/08 and 23/11/2020, taken from the CSN catalog (Barrientos, 2018) and mostly showing the 2020 Atacama sequence (Klein et al., 2021). Black circles show earthquakes from our catalog, starting on 23/11/2020. Beachballs show lower-hemisphere projections of focal mechanisms for events with magnitude $\geq$4.8, taken from GEOFON. Purple contours mark the location of aseismic slip during the 2014 SSE (Klein, Duputel, et al., 2018), the red dot marks the approximate position of the 2020 SSE (Klein et al., 2023). The latitudinal range of earthquake swarms in 1973, 1979, 2006 and 2015 (Ojeda et al., 2023) is indicated by the green bracket, and the pink ellipse shows where non-volcanic tremor was identified in 2019 (Pastén-Araya et al., 2022). Green, yellow and orange lines mark locking degree contour lines of 0.6, 0.7 and 0.8. (right) Plot of earthquake latitudes against time, showing CSN catalog earthquakes in blue and our catalog in black. A horizontal stripe of increased seismicity is present at the latitude of the 2020 Atacama sequence. The red stripe marks the 2020 SSE.

Supporting Information for "Relation between oceanic plate structure, patterns of interplate locking and microseismicity in the 1922 Atacama Seismic Gap"

Diego González-Vidal[1], Marcos Moreno[2], Christian Sippl[3], Juan Carlos Baez[4], Francisco Ortega-Culaciati[5], Dietrich Lange[6], Frederik Tilmann[7,12], Anne Socquet[8], Jan Bolte[9], Joaquin Hormazabal[5], Mickael Langlais[8], Catalina Morales-Yáñez[10], Daniel Melnick[1], Roberto Benavente[10,11], Rodolfo Araya[13]

[1]Institute of Earth Sciences, University Austral of Chile, Valdivia, Independencia 631, 5090000 Valdivia, Chile

[2]Department of Engineering and Geotectonic, Pontifical Catholic University of Chile, Av. Vicuña Mackenna 4860, 8331150 Santiago, Chile

[3]Institute of Geophysics, Czech Academy of Sciences, Bocni II/1401, 14131 Prague, Czech Republic

[4]National Seismological Center, Faculty of Physical and Mathematical Sciences, University of Chile, Av. Beaucheff 1225, 8370583 Santiago, Chile

[5]Department of Geophysics, Faculty of Physical and Mathematical Sciences, University of Chile, Av. Blanco Encalada 2002, 8370449 Santiago, Chile

[6]GEOMAR Helmholtz Centre for Ocean Research Kiel, Wischhofstrasse 1-3, 24098 Kiel, Germany

[7]Department of Geophysics, Deutsches GeoForschungsZentrum GFZ, Wissenschaftpark "Albert Einstein", Telegrafenberg, 14473 Potsdam, Germany

[8]Univ. Grenoble Alpes, Univ. Savoie Mont Blanc, CNRS, IRD, Univ. Gustave Eiffel, ISTerre, 38000 Grenoble, France

[9]Department of Mathematics, University of Kiel, Christian-Albrechts-Platz 4, 24118 Kiel, Germany

March 4, 2023, 7:36pm

[10]Department of Civil Engineering, Universidad Católica de la Santísima Concepción, 4030000 Concepción, Chile

[11]National Research Center for Integrated Natural Disaster Management (CIGIDEN), 8370583 Santiago, Chile.

[12]Institute of Geological Sciences, Freie Universität Berlin, Kaiserswerther Str. 16-18, 14195 Berlin, Germany

[13]Departamento de Ingeniería Matemática CI2MA, Universidad de Concepción, Casilla 160-C, Concepción, Chile

Contents of this file

1. Text S1 to S4
2. Figures S1 to S10
3. Table S1

Additional Supporting Information (Files uploaded separately)

1. Seismicity catalog (comma separated values file)
2. Locking model (netcdf file)
3. GNSS time series (pdf document)
4. GNSS velocity vectors (plain text file)

Text S1: Processing of GNSS time series

We processed the GNSS data using the Bernese 5.2 software (Dach et al., 2015), through a differential approach in network arrangement (Báez et al., 2018), for which we included stations of the network of the International GNSS Service, distributed along South America, and used final orbits and Earth rotation parameters (Teunissen & Montenbruck, 2017). Data were reduced to the absolute phase center of the antenna and we used Vienna Mapping Functions products ("VMF Data Server", 2021) to estimate the tropospheric delays. All free daily solutions were fitted to the IGS weekly solution for November 2022 using a least-squares approach to reduce the effects of datum fixation. We thus obtain the daily positions compatible with ITRF2014, organized in time series of each station. We processed the daily time series for the period between 2018-01-01 and 2023-02-01 using the python package DISSTANS (Köhne et al., 2023). First, we removed the outliers and the common mode error (CME) from the time series using independent component analysis (ICA) (Huang et al., 2012). To estimate the CME, the low-frequency signal was first empirically eliminated, leaving only the high-frequency signals (frequency at which the CME manifests itself), and using the ICA method, the CME was estimated and then removed from the time series.

We then used a trajectory model (Bevis & Brown, 2014) to characterize the motion of the GNSS stations. We fitted a secular and seasonal (semi-annual and annual) component to the data, as well as a step function where offsets (of artificial or tectonic origin) were detected. We also model a logarithmic decay after all earthquakes with M_w >6. In this way, we estimated the velocities of each of the stations in the ITRF2014 system, then

removed the effect of the rigid body rotation of the South American plate at the ITRF2014 velocities and transformed the estimated horizontal displacements and velocities to a reference system with respect to the stable part of the South American plate by subtracting the angular velocity described by the Euler vector of 21.44°S, 125.18°W, 0.12°/Myr. All time series analyzed and modeled with the trajectory model are shown in Table S1 and the data available online.

Text S2: Bayesian inversion of locking degree

We modeled the interseismic deformation using the backslip model of Savage (1983). A finite element model (FEM) was used to generate the unitary dislocations to construct the Green's functions. We calculate the downdip and along-strike components of slip using the Pylith software (Aagaard et al., 2013), assuming a three-dimensional spherical viscoelastic model, following the method and physical properties used by Li, Moreno, Bedford, Rosenau, and Oncken (2015). Thus, the FEM includes topography and bathymetry as well as a realistic geometry of the slab and continental Moho (Hayes et al., 2018). The fault is configured by triangular elements and the slip is estimated at each node (vertex of each element). The distance between the centers of the subfaults on the fault is about 20-30 km, consisting of 600 nodes between 21°S and 32°S.

For the inversion of the observational data, i.e., velocity at each of the GNSS sites, we use the reversible jump Markov Chain Monte Carlo (rj-MCMC) method which is a sampler for transdimensional problems. The rj-MCMC method is a generalization of the Metropolis-Hastings algorithm that allows dimension jumps. The main idea of the MCMC method is that a Markov process is used to generate samples M from the target

distribution $p(M|D,I)$ which spans the entire model space and that asymptotically reaches a stationary distribution. The quantity $p(M|D,I)$ denotes the conditional probability of the model M of the slip distribution w.r.t. observational GNSS data D given background information I. It can be computed via Bayes' theorem as

$$p(M|D,I) = \frac{p(M|I)\,p(D|M,I)}{p(D|I)} \tag{1}$$

with the prior $p(M|I)$ and the so-called marginal probability $p(D|I)$ which serves as a normalization constant. In the following we simply write $p(M|D)$ instead of $p(M|D,I)$ to simplify the notation, with I being assumed implicitly.

The conditional probability $p(D|M)$ can be interpreted as the likelihood $L(M|D)$ of model M given the fixed displacements D. Assuming Gaussian errors, as we do for our model, there holds

$$p(D|M) = L(M|D) \propto \exp\left[-\frac{1}{2}\sum_{i=1}^{n}\frac{(D_i - (G\,M)_i)^2}{\sigma_i^2}\right], \tag{2}$$

where D_i, $i = 1,\ldots,n$, are the observed displacements, G is the $(n \times m)$ Green's function matrix, M_j, $j = 1,\ldots,m$, is the slip at the fault nodes and σ_i^2 is the variance which is assumed to be 1.

Combining (1) with (2) yields finally the desired probability of a slip distribution M

$$p(M|D) \propto \exp\left[-\frac{1}{2}\sum_{i=1}^{n}(D_i - (G\,M)_i)^2\right]. \tag{3}$$

In the Metropolis–Hastings algorithm the transition probabilities $p(\tilde{M}|M)$ from state M to any other state $\tilde{M}$ are constructed such that after an initial burn-in period it generates samples with a probability density equal to the desired posterior $p(M|D)$. For it we

assume the detailed balance

$$p(\tilde{M}|M)\,p(M|D) = p(M|\tilde{M})\,p(\tilde{M}|D) \tag{4}$$

and that the transition probability can be written as the product of the *proposal distribution* $q(\tilde{M}|M)$, the conditional probability of state $\tilde{M}$ given M, and the *acceptance distribution* $a(\tilde{M}|M)$, the probability to accept the proposed model $\tilde{M}$, i.e.,

$$p(\tilde{M}|M) = q(\tilde{M}|M)\,a(\tilde{M}|M). \tag{5}$$

Combining (4) and (5) yields the *Metropolis ratio*

$$r(\tilde{M}, M) = \frac{p(\tilde{M}|D)\,q(M|\tilde{M})}{p(M|D)\,q(\tilde{M}|M)}$$

and the acceptance probability

$$a(\tilde{M}|M) = \min(1, r) = \min\left(1, \frac{p(\tilde{M}|D)\,q(M|\tilde{M})}{p(M|D)\,q(\tilde{M}|M)}\right).$$

Hereinafter, we assume a symmetric proposal distribution, i.e., $q(M|\tilde{M}) = q(\tilde{M}|M)$, such that the Metropolis ratio reduces to

$$r(\tilde{M}, M) = \frac{p(\tilde{M}|D)}{p(M|D)}.$$

The Metropolis–Hastings algorithm reads then:

1. Initialize a slip distribution M^0 and set $t = 0$.
2. `REPEAT UNTIL` the probability density of the states $M^0, \ldots, M^t$ converges to a stationary distribution
    1. Generate a new slip distribution $\tilde{M}$ from $q(\tilde{M}|M^t)$.
    2. Generate an uniform random variable $u \in [0, 1]$.
    3. `IF` $u \leq r(\tilde{M}, M^t)$

Set $M^{t+1} = \tilde{M}$.

4. ELSE

Set $M^{t+1} = M^t$.

5. Set $t = t + 1$.

rj-MCMC method applied to Voronoi cell parametrization

The rj-MCMC method (Green, 1995; Bodin & Sambridge, 2009) is an extension of the MCMC method which uses for the inversion, instead of the n fault nodes, $k \leq n$ Voronoi cells that parameterize slip behavior across the megathrust fault using a piece-wise constant slip representation (i.e., constant slip inside each Voronoi cell). Hence, instead of the slip model $M = (M_j)_{j=1,\dots,m}$ for the fault nodes a slip model $X = (X_i)_{i=1,\dots,k}$ for the centers of the Voronoi cells is used. The idea of the rj-MCMC method is that the number and location of the Voronoi cell centers is not fixed but is also varied by a stochastic process. Therefore, in every iteration step randomly a cell center k is chosen for which one of the following modifications are performed with the same probability:

1. change of one slip component,
2. move the cell center, i.e., random perturbation of the cell center location,
3. remove the cell center.

Moreover, as a further possibility also

4. add a new cell center with a random location on the fault surface and set its slip to a random perturbation of the slip of its nearest neighbor,

is allowed. After any of these modifications the Metropolis ratio $r(\tilde{X}, X)$ of the new model $\tilde{X}$ and the old model X is computed to accept or to reject the new model. At the end the slip model X of the cell centers is mapped to a slip model M of the fault nodes.

Parallel tempering

If the target probability distribution is multi-modal, the (rj-)MCMC method can become stuck in a local mode and will never explore other modes. To efficiently sample this high dimensional problem, we employ the *parallel tempering* (Sambridge, 2013) where multiple copies/chains of the iteration are run in parallel, each with a different "temperature" T. For them the Metropolis ratio reads

$$r(\tilde{X}, X, T) = \left(\frac{p(\tilde{X}|D, I)}{p(X|D, I)} \right)^{1/T}$$

such that for $T = 1$ we obtain the desired target probability distribution, while higher temperatures will sample a smooth version of it. Thus, chains with high temperatures are unlikely to be trapped in local maxima and are allowed to explore the space with more freedom. Note that only the samples drawn from chains at T =1 are utilized later to characterize the posterior. After a fixed number of iterations two chains with temperature T_X and $T_{\tilde{X}}$ are exchanged if for an uniform random variable $u \in [0, 1]$ there holds

$$u \leq \frac{p(X|D, I)^{1/T_X}\, p(\tilde{X}|D, I)^{1/T_{\tilde{X}}}}{p(\tilde{X}|D, I)^{1/T_X}\, p(X|D, I)^{1/T_{\tilde{X}}}} = r(\tilde{X}, X, T_{\tilde{X}}, T_X).$$

Algorithm

Combining all the information given above, we can write down the algorithm for the Bayesian inversion:

1. Initialize a slip distribution M^0, set $t = 0$ and set temperatures T_j for $j = 1, \ldots, J$.
2. Define the Voronoi cell centers and map M^0 to its slip distribution X^0.
3. Set $X^{0,j} = X^0$ for $j = 1, \ldots, J$.
4. `REPEAT UNTIL` $|\|D - G\, M^t\| - \|D - G\, M^{t+s}\|| <$ TOL for all $s \leq S$
    1. `FOR` $j = 1, \ldots, J$ `DO`

1. `FOR` $\ell = 0, \ldots, L$ `DO`
    1. Generate a new slip distribution $\tilde{X}$ by either

    (i) changing one slip component of $X^{\ell,j}$,

    (ii) moving the center of a Voronoi cell,

    (iii) removing the cell center,

    (iv) or adding a new Voronoi cell.

    2. Generate an uniform random variable $u \in [0, 1]$.
    3. `IF` $u \leq r(\tilde{X}, X^{\ell,j}, T_j)$

        Set $X^{\ell+1,j} = \tilde{X}$.

    `ELSE`

        Set $X^{\ell+1,j} = X^{\ell,j}$.

    4. Set $\ell = \ell + 1$.
2. For all $j = 1, \ldots, J$ map $X^{L,j}$ to the slip distribution $M^{t,j}$ of the fault nodes.
3. For all pairs $(j, j+1)$ generate uniform random variables $u \in [0, 1]$.
4. `IF` $u \leq r(M^{t,j}, M^{t,j+1}, T_j, T_{j+1})$

    Exchange for chain j with chain $j + 1$.
5. Find i with $T_i = 1$ and set $M^{t+1} = M^{t,i}$.
6. Set $t = t + 1$.
7. Set $X^{0,j} = X^{L,j}$ for $j = 1, \ldots, J$.

Text S3: Earthquake detection and location workflow

We deployed a dense network of 60 seismic stations (network code Y6-2020-2022; (Tilmann et al., 2021)) in the framework of the Anillo PRECURSOR project (Figure 1). Data from this temporal network, which operated between November 2020 and July 2022,

and recorded ∼988Gb of continuous 3-component data with a sampling rate of 100 Hz, formed the backbone of the performed analysis. It consisted of 20 short-period seismometers (Mark-L4C), 20 broadband seismometers (Trillium compact) and 20 geophones with 4.5Hz corner frequency (3D PE-6/B) deployed onshore. We complemented these data with 25 seismic stations from the temporary network DeepTrigger Chile (XZ 2020-2024) operated by ISTerre between 26.5°S and 30.3°S and further 16 stations from regional permanent networks (network codes CX (GFZ & CNRS-INSU, 2006), C1 (Universidad de Chile, 2013), C (no DOI available) and IU (Albuquerque Seismological Laboratory/USGS (ASL), 2014). The data availability is shown in Figure S6.

For detecting earthquakes and picking their P- and S- phases on single stations, we used the deep learning-based code EQTransformer (Mousavi et al., 2020) via the SeisBench platform (Münchmeyer et al., 2022; Woollam et al., 2022), which was pre-trained with the STEAD dataset that contains more than 1.3 million events in local and regional distances (Mousavi et al., 2019). Mousavi et al. (2020) showed that this model is less sensitive to different background noise levels and works well for small events with different waveform shapes and high background noise. We pre-processed the daily waveforms by filling the gaps, removing the trend, band-pass filtering 1-45 Hz and re-sampling the data to 100 Hz. We then applied EQTransformer to 6h length traces. The algorithm first scans the entire data for events, and only attempts to pick P- and S-arrivals where an event has been declared. We used probability thresholds of 0.04, 0.075 and 0.1 for event detection, P- and S-phase picking. For associating the picked phases to events with initial hypocenters, we used the deep learning phase associator GaMMA (Zhu et al., 2022). Events were

required to feature at least 7 P- and 4 S-phases. A grid of 750 km $\times$ 1400 km with a grid spacing of $\sim$4 km and a constant velocity model with Vp = 7 km/s and Vp/Vs = 1.74 were used for deriving theoretical travel times. Retrieved events were then relocated with NonLinLoc in the 2D velocity model of Sippl, Schurr, Asch, and Kummerow (2018), which was derived for the region north of Antofagasta city. We thus obtained a catalog containing 30,560 events, 469,980 P-phases and 391,350 S-phases, which we refer to as the preliminary catalog (Figure S7). Average location errors derived from the standard deviation of NonLinLoc's probability density function is < 5 km inside the network and increases toward the trench and volcanic arc up to $\sim 10 - 25$km (Figure S8).

In the next step, we determined a local minimum 1D velocity model using the program VELEST (Kissling et al., 1994) with a subset of 1651 well-constrained events that were selected based on the number of picks and their location within the station network. A wide variety of different 1D starting models was employed for the inversion, which converged toward the 1D model we chose. The entire catalog was then jointly relocated in this 1D model with VELEST, also inverting for station corrections. Picks with residuals further than two standard deviations from the event's mean residual were removed in this step. Next, we inverted for a 2D velocity model using the algorithm simul2000 (e.g. Thurber & Eberhart-Phillips, 1999), again with the smaller set of well-constrained events and using the previously determined minimum 1D model as starting model. The optimal damping for the inversion was determined by the analysis of trade-off curves. All events were relocated in the resulting 2D velocity model. We then cross-correlated waveforms around P- and S-wave catalog picks at common stations for event pairs separated by less

than 15 km both horizontally and in depth. The correlated waveforms were taken from 0.5 s before to 1.5 s after the catalog pick for P, and from 1.5 s before to 2.5 s after the catalog pick for S-arrivals, and the data was bandpass filtered between 1 and 10 Hz (P) and 0.5 and 6 Hz (S), respectively. We only kept lag times for event pairs and stations where the cross-correlation (CC) coefficient exceeded 0.7, and only kept the event pair if a CC coefficient >0.7 was obtained for at least four observations. These lag times, together with traveltime differences from the catalog picks, served as input for the final double-difference relocation step using hypoDD (Waldhauser & Ellsworth, 2000). The entire catalog was relocated using 1,726,699 P- and 1,314,770 S-traveltime differences from the catalog as well as 261,816 P- and 71,843 S-wave cross-correlation lagtimes. The weighting scheme between these inputs was designed to initially place most weight on the catalog arrivals, then gradually upweighting the cross-correlation lagtimes through a total of 15 iterations. Overall, RMS residuals of arrival time differences were reduced from 0.189 to 0.105 s (-44%) for the catalog-derived traveltime differences and from 0.26 to 0.051 s (-80%) for the cross-correlation lagtimes.

We determined local magnitudes of each event by using the software SEISAN (Havskov et al., 2020). Amplitudes (A) were automatically determined for the picked stations and the local magnitude of an earthquake was computed as the median of the station magnitudes, using the period range $<$ 5s at hypocentral distances $d <$ 300km, with the equation for local magnitudes:

$$M_l = \log_{10}(A) + 1.11 \log_{10}(d) + 0.00189d - 2.09. \quad (6)$$

In this catalog, local magnitudes range from 0.6 to 5.7 and we obtain an overall completeness magnitude of 1.6 and a b-value of 0.89 estimated with the method of Mizrahi, Nandan, and Wiemer (2021) (Figure 2 and S9).

Text S4: Searching for repeating earthquakes

We searched our dataset for repeating earthquakes by computing the waveform cross-correlation in a time window from 5 s before to 30 s after the catalog P-arrival and filtering between 1 Hz and 5 Hz. Then, we use the criterion of (Uchida & Matsuzawa, 2013) that two events belong to a "repeater family" if they achieve a cross-correlation coefficient larger than 0.95 at two or more stations. Investigating only event pairs with less than 8 km horizontal and <12 km vertical separation, and only keeping repeater families with four or more events yielded a total of 148 repeater families comprising 1379 events (Figure 2). It should be noted that with this procedure, we can not assess whether what we obtain are repeaters in the strict sense, which re-rupture the exact same patch. Most of these events are likely just highly similar events occurring in close proximity to each other, and whose rupture dimensions may or may not overlap. As such, they still function as a proxy for the presence of aseismic slip, but can not be used for quantitative estimates of slip rate.

References

Aagaard, B. T., Knepley, M. G., & Williams, C. A. (2013). A domain decomposition approach to implementing fault slip in finite-element models of quasi-static and dynamic crustal deformation. *Journal of Geophysical Research: Solid Earth*, *118*(6), 3059-3079. Retrieved from https://agupubs.onlinelibrary.wiley.com/

doi/abs/10.1002/jgrb.50217 doi: 10.1002/jgrb.50217

Albuquerque Seismological Laboratory/USGS (ASL). (2014). *Global Seismograph Network (GSN - IRIS/USGS) [Dataset].* Federation of Digital Seismograph Networks. doi: https://doi.org/10.7914/SN/IU

Bevis, M., & Brown, A. (2014). Trajectory models and reference frames for crustal motion geodesy. *Journal of Geodesy*, *88*, 283–311. doi: 10.1007/s00190-013-0685-5

Bodin, T., & Sambridge, M. (2009). Seismic tomography with the reversible jump algorithm. *Geophysical Journal International*, *178*, 1411-1436.

Báez, J. C., Leyton, F., Troncoso, C., del Campo, F., Bevis, M., Vigny, C., ... Blume, F. (2018). The Chilean GNSS Network: Current Status and Progress toward Early Warning Applications. *Seismological Research Letters*, *89*(4), 1546-1554. doi: 10 .1785/0220180011

Dach, R., Lutz, S., Walser, P., & Fridez, P. e. (2015). Bernese GNSS Software Version 5.2. In *University of Bern, Bern Open Publishing.* doi: 10.7892/boris.72297

GFZ, & CNRS-INSU. (2006). *IPOC Seismic Network: Integrated Plate boundary Observatory Chile - IPOC.* GFZ Data Services. doi: 10.14470/PK615318

Green, P. J. (1995). Reversible jump Markov chain Monte Carlo computation and Bayesian model determination. *Biometrika*, *82*, 711-732.

Havskov, J., Voss, P. H., & Ottemöller, L. (2020, 03). Seismological Observatory Software: 30 Yr of SEISAN. *Seismological Research Letters*, *91*(3), 1846-1852. doi: 10.1785/0220190313

Hayes, G. P., Moore, G., Portner, D. E., Hearne, M., Flamme, H., Furtney, M., &

Smoczyk, G. M. (2018). Slab2, a comprehensive subduction zone geometry model. *Science*, *362*(6410), 58–61. doi: 10.1126/science.aat4723

Huang, D., Dai, W., & Luo, F. (2012, 10). Ica spatiotemporal filtering method and its application in gps deformation monitoring. *Applied Mechanics and Materials*, *204-208*, 2806-2812. doi: 10.4028/www.scientific.net/AMM.204-208.2806

Kissling, E., Ellsworth, W. L., Eberhart-Phillips, D., & Kradolfer, U. (1994). Initial reference models in local earthquake tomography. *Journal of Geophysical Research*, *99*(B10), 19,635–19,646.

Köhne, T., Riel, B., & Simons, M. (2023). Decomposition and inference of sources through spatiotemporal analysis of network signals: The disstans python package. *Computers & Geosciences*, *170*, 105247. doi: https://doi.org/10.1016/j.cageo.2022.105247

Li, S., Moreno, M., Bedford, J., Rosenau, M., & Oncken, O. (2015). Revisiting viscoelastic effects on interseismic deformation and locking degree: A case study of the peru-north chile subduction zone. *Journal of Geophysical Research: Solid Earth*, *120*(6), 4522-4538. doi: https://doi.org/10.1002/2015JB011903

Lomax, A., Virieux, J., Volant, P., & Berge-Thierry, C. (2000). Probabilistic Earthquake Location in 3D and Layered Models. In *Advances in seismic event location* (pp. 101–134). doi: 10.1007/978-94-015-9536-0_5

Mizrahi, L., Nandan, S., & Wiemer, S. (2021). The effect of declustering on the size distribution of mainshocks. *Seismological Research Letters*, *92*, 2333–2342. doi: https://doi.org/10.1785/0220200231

Mousavi, S. M., Ellsworth, W. L., Zhu, W., Chuang, L. Y., & Beroza, G. C. (2020).

Earthquake transformer—an attentive deep-learning model for simultaneous earthquake detection and phase picking. *Nature Communications*, *11*. doi: 10.1038/s41467-020-17591-w

Mousavi, S. M., Sheng, Y., Zhu, W., & Beroza, G. C. (2019). STanford EArthquake Dataset (STEAD): A Global Data Set of Seismic Signals for AI. *IEEE Access*, *7*, 179464–179476. Retrieved from `http://dx.doi.org/10.1109/ACCESS.2019.2947848` doi: 10.1109/access.2019.2947848

Münchmeyer, J., Woollam, J., Rietbrock, A., Tilmann, F., Lange, D., Bornstein, T., ... Soto, H. (2022). Which picker fits my data? a quantitative evaluation of deep learning based seismic pickers. *Journal of Geophysical Research: Solid Earth*, *127*. doi: 10.1029/2021JB023499

Sambridge, M. (2013, 10). A Parallel Tempering algorithm for probabilistic sampling and multimodal optimization. *Geophysical Journal International*, *196*(1), 357-374. doi: 10.1093/gji/ggt342

Savage, J. C. (1983). A dislocation model of strain accumulation and release at a subduction zone. *Journal of Geophysical Research: Solid Earth*, *88*(B6), 4984-4996. doi: https://doi.org/10.1029/JB088iB06p04984

Sippl, C., Schurr, B., Asch, G., & Kummerow, J. (2018). Seismicity structure of the northern chile forearc from >100,000 double-difference relocated hypocenters. *Journal of Geophysical Research: Solid Earth*, *123*, 4063-4087. doi: 10.1002/2017JB015384

Teunissen, P. J., & Montenbruck, O. (2017). *Springer Handbook of Global Navigation Satellite Systems*. Springer Cham. doi: https://doi.org/10.1007/978-3-319-42928-1

Thurber, C. H., & Eberhart-Phillips, D. (1999). Local earthquake tomography with flexible gridding. *Computers and Geosciences*, *25*(7), 809–818. doi: 10.1016/S0098-3004(99)00007-2

Tilmann, F., Heit, B., Moreno, M., & González-Vidal, D. (2021). *Anillo.* GFZ Data Services. doi: 10.14470/L17575324477

Uchida, N., & Matsuzawa, T. (2013). Pre- and postseismic slow slip surrounding the 2011 Tohoku-oki earthquake rupture. *Earth and Planetary Science Letters*, *374*, 81-91. doi: 10.1016/j.epsl.2013.05.021

Universidad de Chile. (2013). *Red Sismologica Nacional. International Federation of Digital Seismograph Networks.* doi: https://doi.org/10.7914/SN/C1

VMF Data Server. (2021). In *re3data.org: Vmf data server; editing status 2021-08-24; re3data.org - registry of research data repositories.* doi: http://doi.org/10.17616/R3RD2H

Waldhauser, F., & Ellsworth, W. L. (2000). A Double-difference Earthquake location algorithm: Method and application to the Northern Hayward Fault, California. *Bulletin of the Seismological Society of America*, *90*(6), 1353–1368. doi: 10.1785/0120000006

Woollam, J., Münchmeyer, J., Tilmann, F., Rietbrock, A., Lange, D., Bornstein, T., ... Soto, H. (2022). SeisBench—A Toolbox for Machine Learning in Seismology. *Seismological Research Letters*, *93*(3), 1695-1709. doi: 10.1785/0220210324

Yáñez-Cuadra, V., Ortega-Culaciati, F., Moreno, M., Tassara, A., Krumm-Nualart, N., Ruiz, J., ... Benavente, R. (2022). Interplate Coupling and Seismic Potential in

the Atacama Seismic Gap (Chile): Dismissing a Rigid Andean Sliver. *Geophysical Research Letters*, 1–26. doi: 10.1029/2022gl098257

Zhu, W., McBrearty, I. W., Mousavi, S. M., Ellsworth, W. L., & Beroza, G. C. (2022). Earthquake phase association using a bayesian gaussian mixture model. *Journal of Geophysical Research: Solid Earth*, *127*(5), e2021JB023249. (e2021JB023249 2021JB023249) doi: https://doi.org/10.1029/2021JB023249

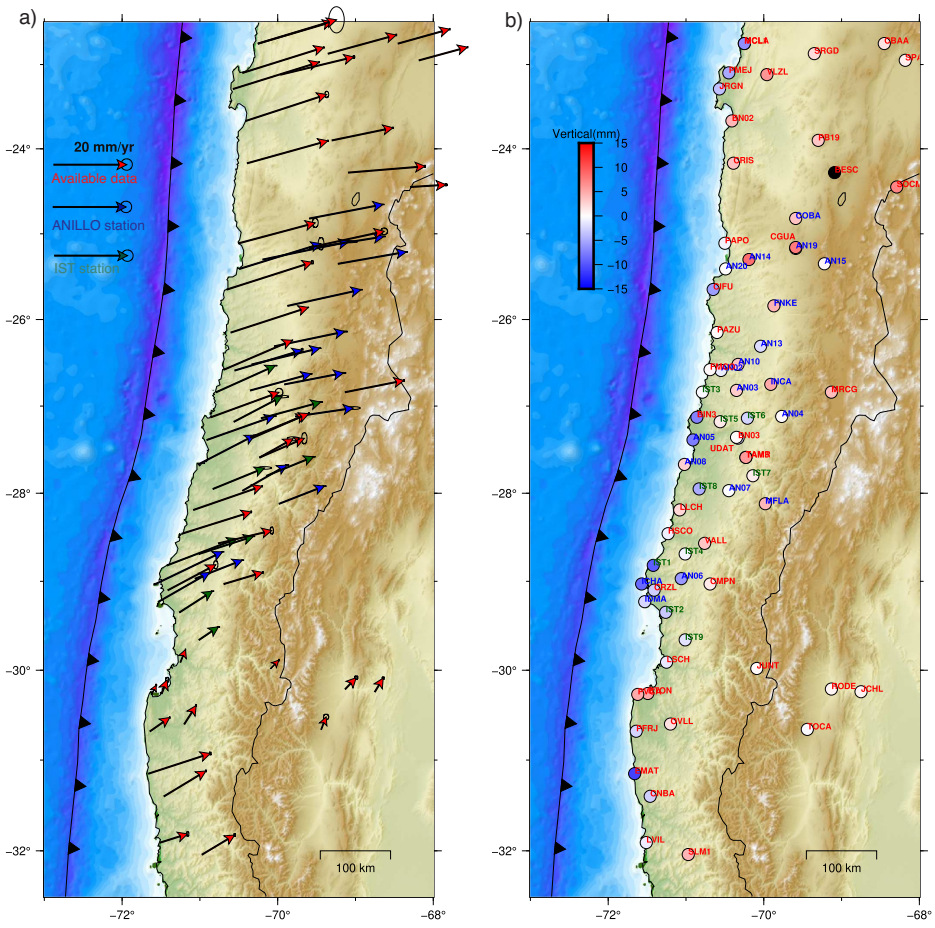

Figure S1. Combined GNSS network, with obtained horizontal (a) and vertical velocities (b) representing the period between 2018 to 2022 (70 stations). Existing CSN Chile open access stations (42 stations) are shown by vectors and red labels in (a) and (b). New stations installed by the ANILLO (19 stations) and Deep-Trigger projects (9 stations) are represented by blue and green vectors and labels in a) and b), respectively.

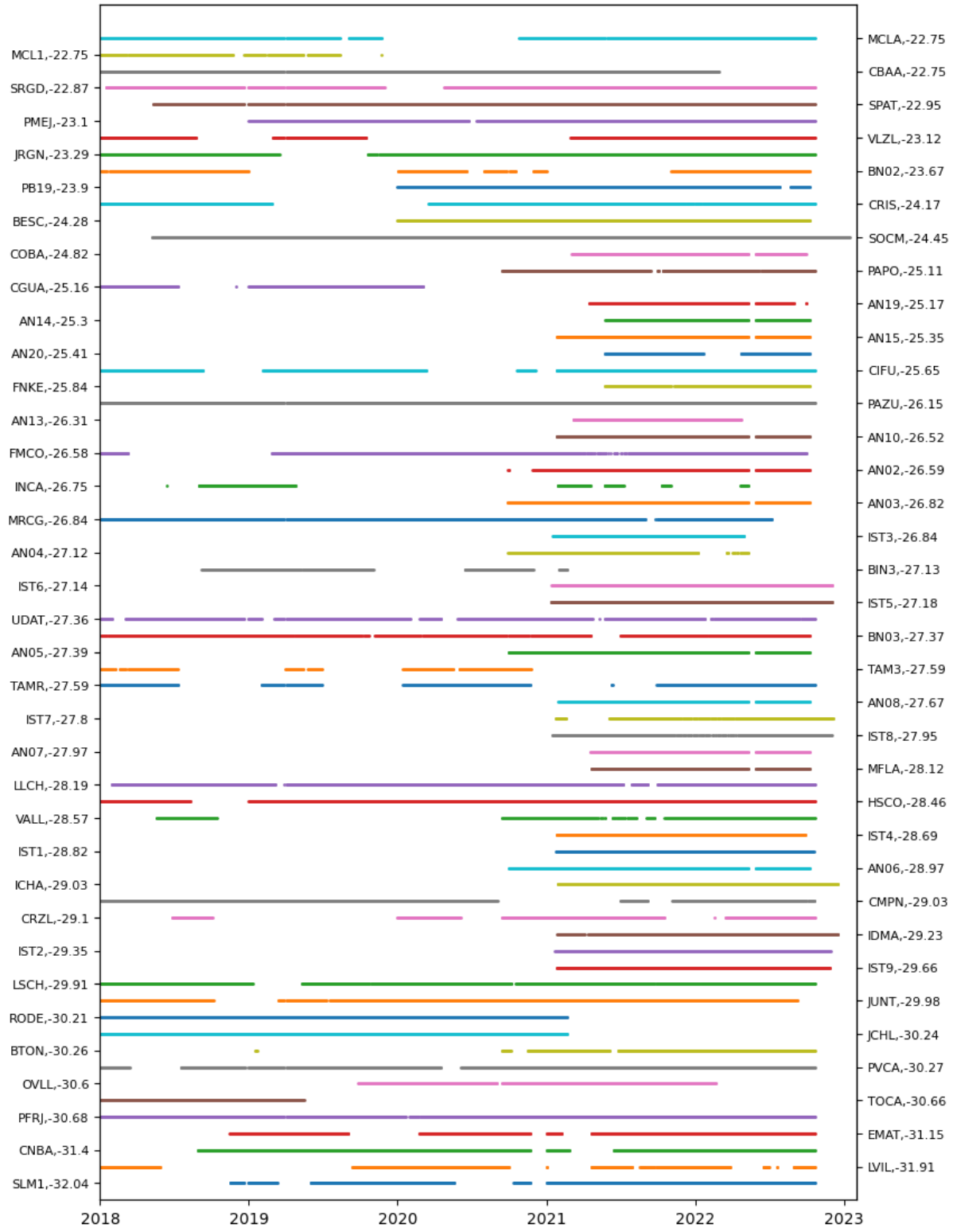

Figure S2. Data availability of GNSS stations. Stations are sorted by latitude, which is given for each station next to its name.

March 4, 2023, 7:36pm

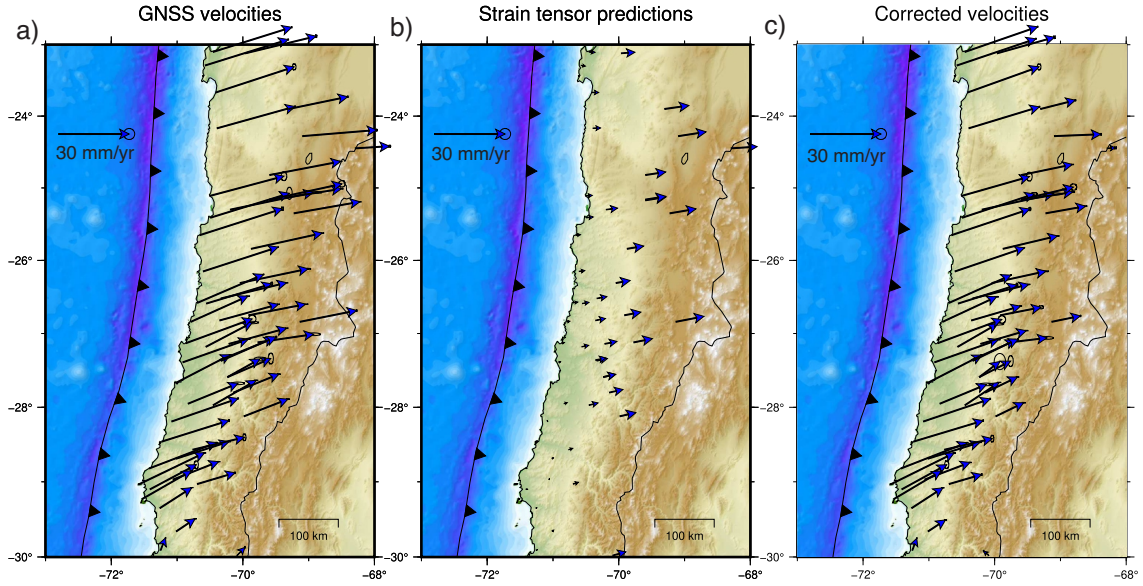

Figure S3. a) GNSS velocities relative to the stable part of the South American continent. b) Continental deformation derived from Yáñez-Cuadra et al. (2022) based on the deformation tensor. These displacements are subtracted from the velocities in (a) to obtain a displacement field for the locking degree inversion (c).

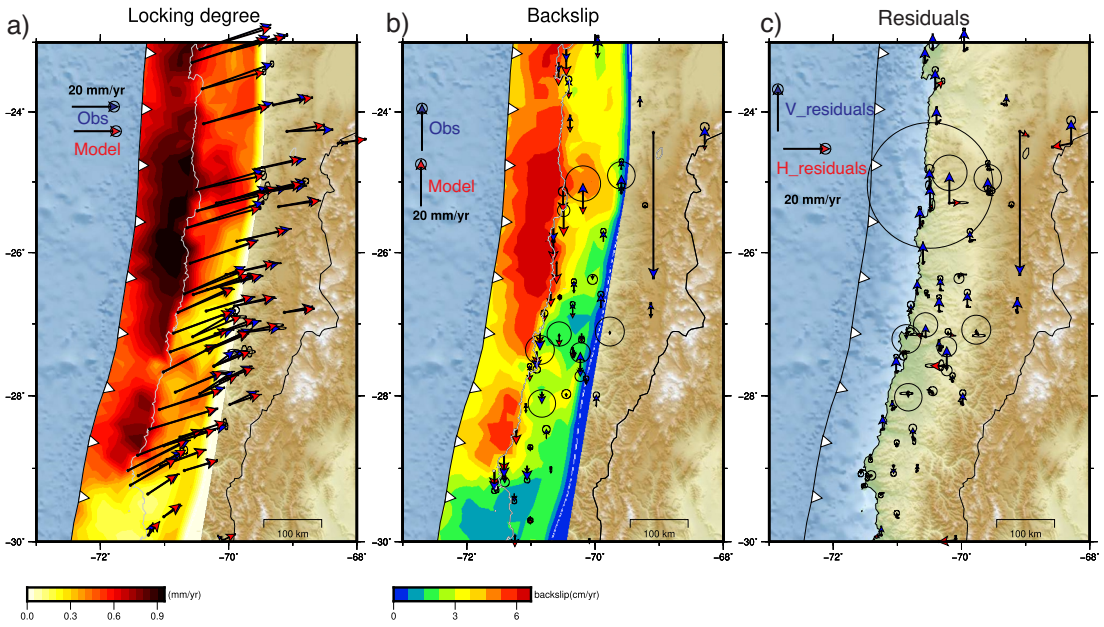

Figure S4. Summary of results for the locking model inversion. a) The obtained distribution of locking degree, with observed (blue vectors) and predicted (red vectors) horizontal displacements. b) Obtained backslip and observed (blue vectors) and predicted (red vectors) vertical displacements. c) Horizontal (red vectors) and vertical (blue vectors) displacement residuals.

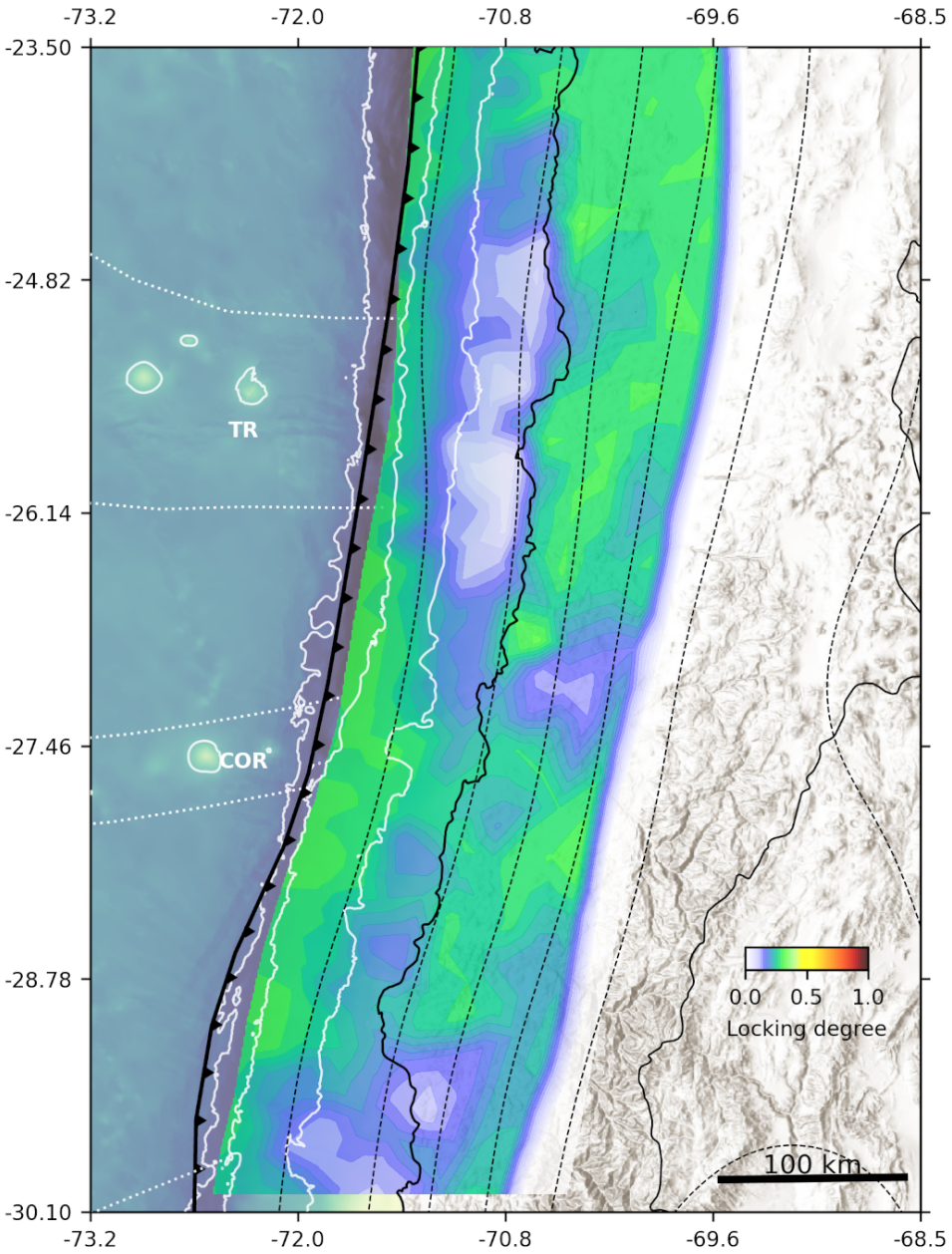

Figure S5. Standard deviation of the final ensemble of locking model estimations, obtained with the transimensional MCMC approach. This can be represents the posterior uncertainty of the slip model.

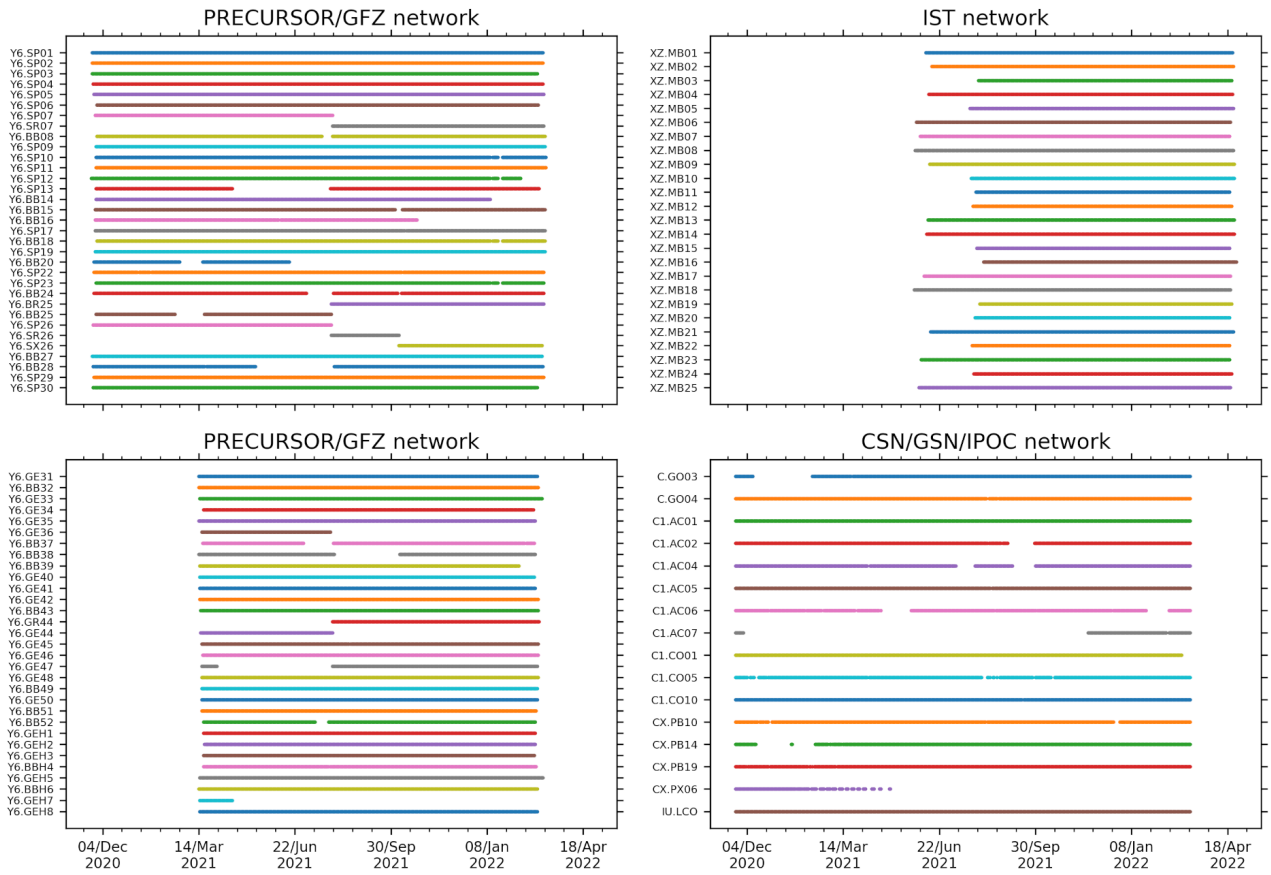

Figure S6. Data availability of seismic stations. Stations are sorted by network and name.

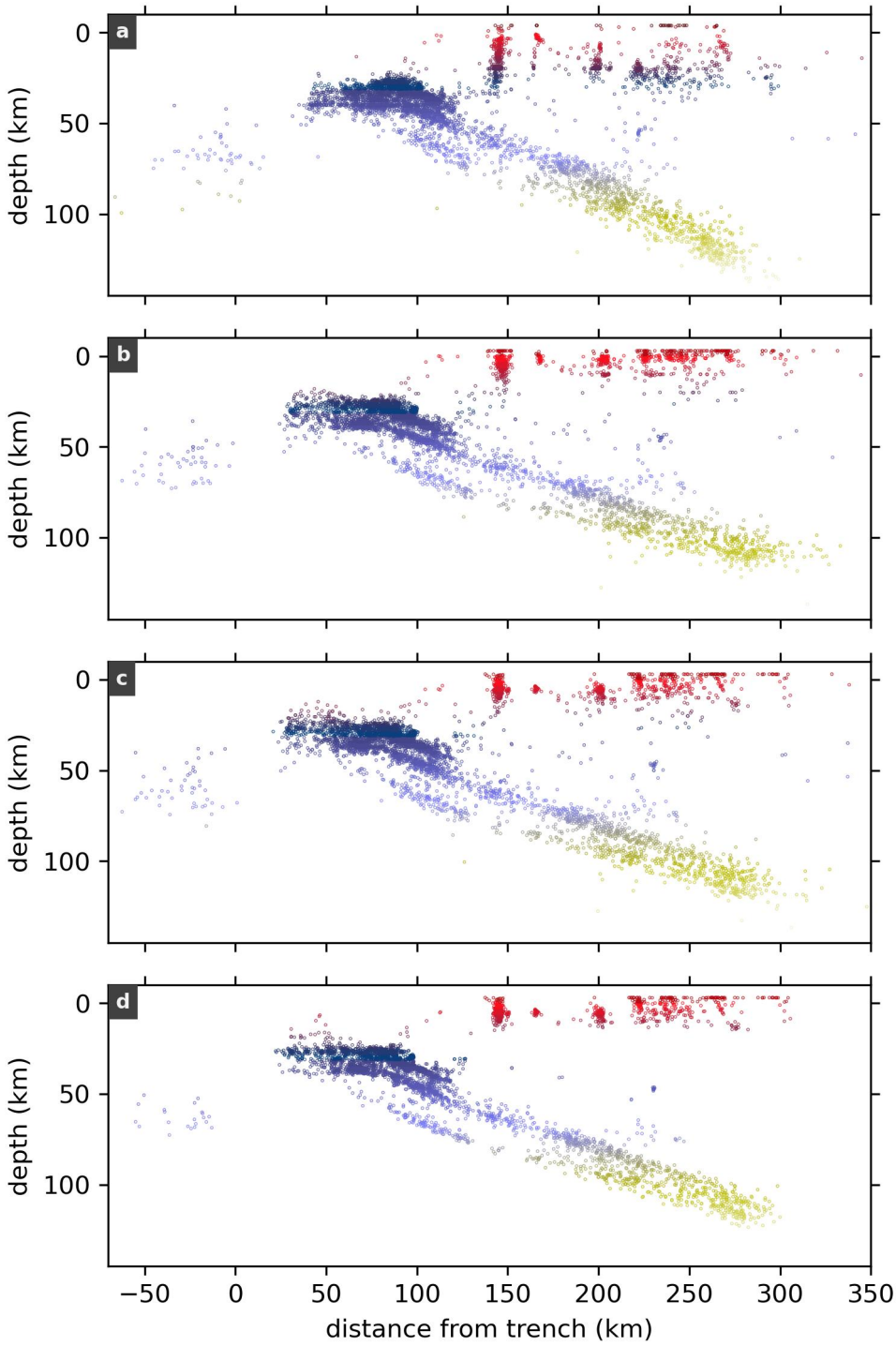

Figure S7. Different stages of catalog evolution from the preliminary catalog (subfigure a) to the relocalized catalog using a minimum 1D velocity model and station corrections (subfigure b), then using a minimum 2D velocity model (subfigure c) and finally the double-difference relocalized catalog (subfigure d).

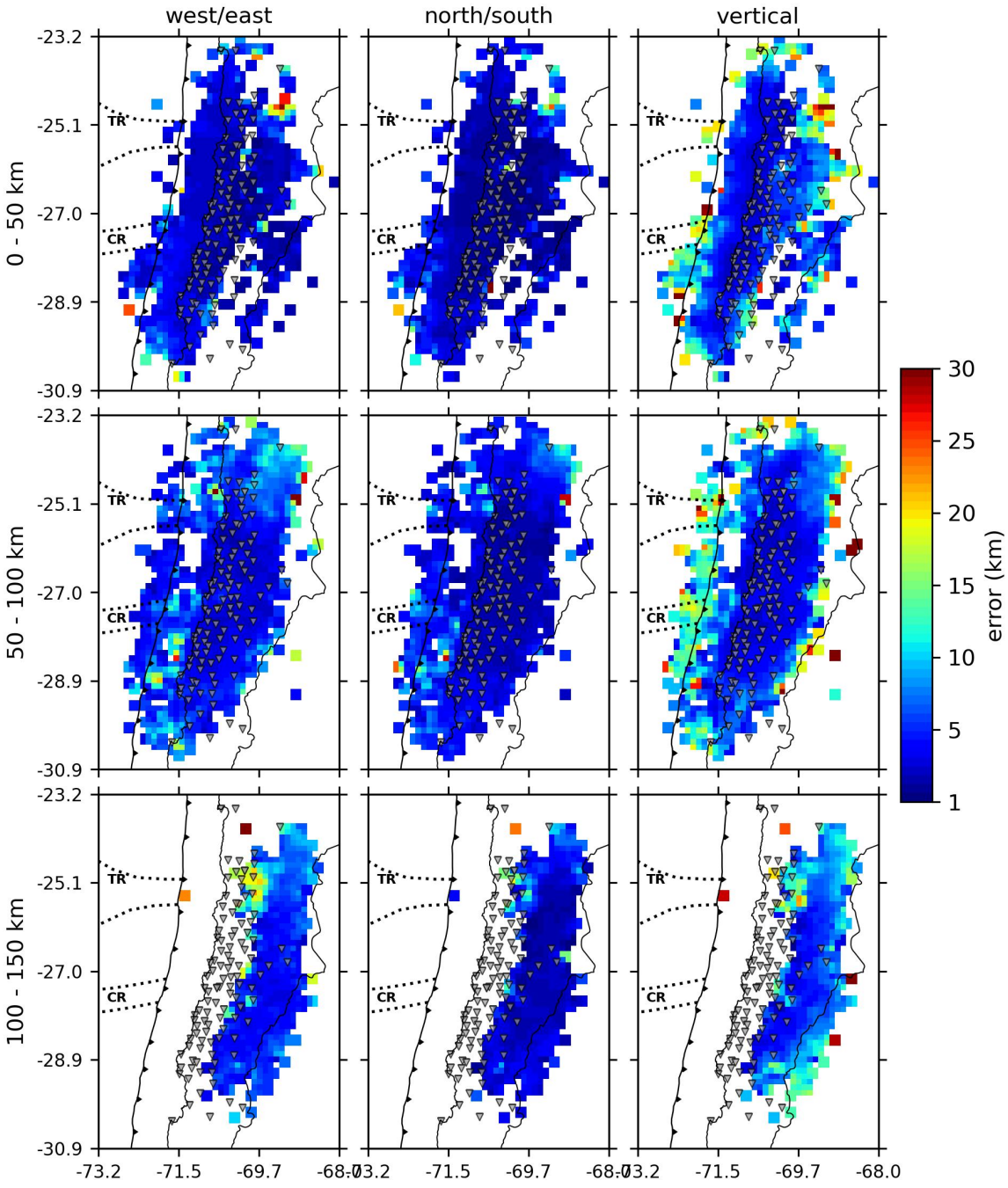

Figure S8. Estimates of absolute location errors, obtained by probabilistic relocation using NonLinLoc (Lomax et al., 2000). For each grid cell, we averaged the obtained standard deviations of the location probability density distribution. While small values (<5 km) prevail inside the seismometer network, regions updip and downdip of the network feature larger uncertainties, especially in depth.

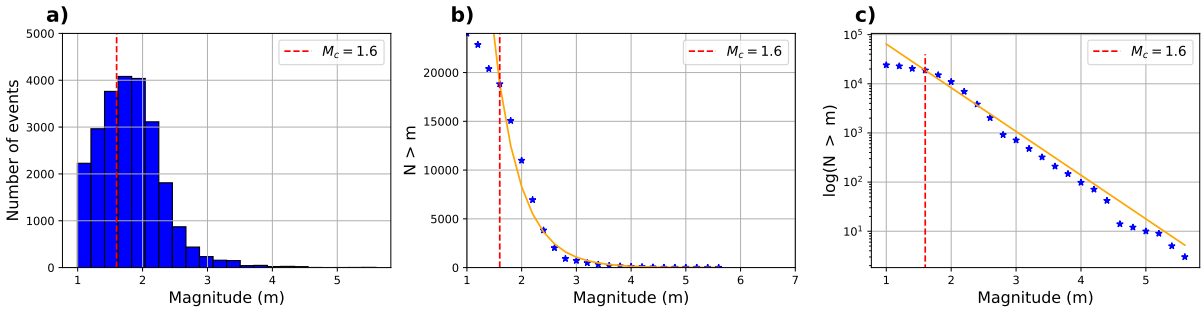

Figure S9. Completeness magnitude estimation. a) Histogram of the frequency of the earthquakes as a function of magnitude. b) Cumulative earthquake numbers (blue) and the Gutenberg-Richter equation that best fits the observations (orange). c) Logarithmic version of (b).

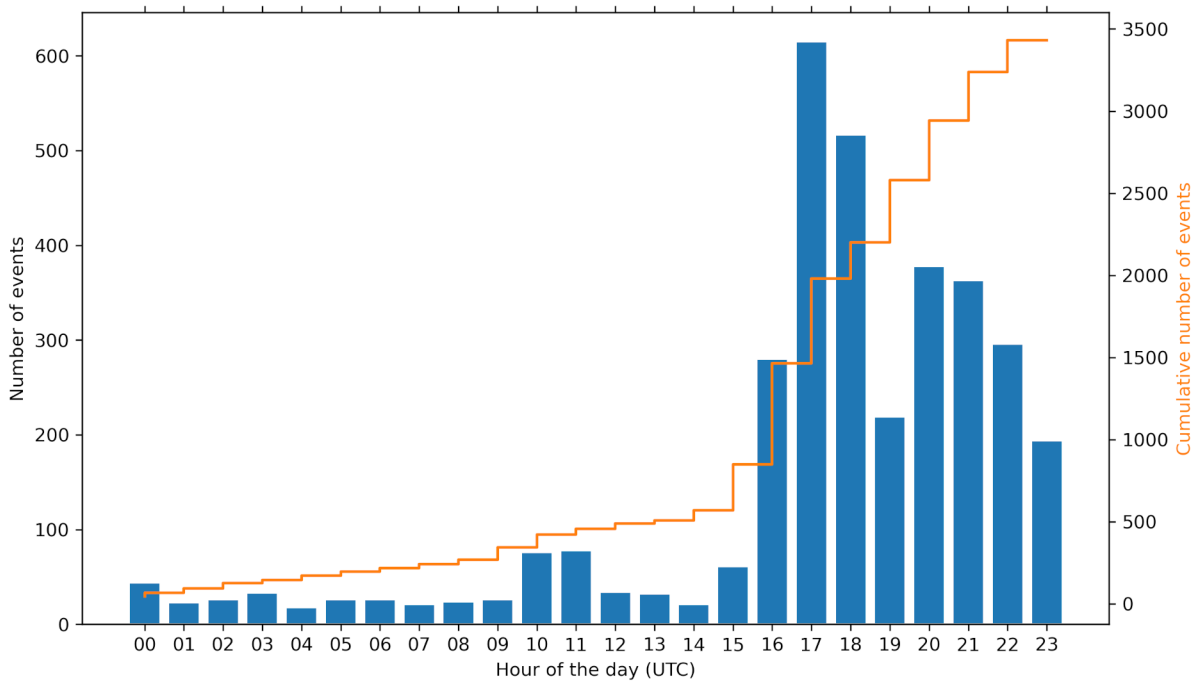

Figure S10. Distribution of upper plate seismicity against time. The occurrence rate of upper plate seismicity is significantly increased between 16:00 and 23:00 UTC time (i.e., 12:00 and 20:00 local time) likely due to mining blast activity

Table S1. GNSS velocity vectors and errors in mm/yr. The columns show the name, longitude, latitude, velocity East/West, velocity North/South, Velocity up/down, error East-West, error North/South and error up/down for each GNSS station (part 1/4).

Name	Lon(°)	Lat(°)	VelEW	VelNS	VelUP	ErrEW	ErrNS	ErrUP
AN02	-70.55	-26.59	27.652317	8.370159	-1.180043	0.357906	0.631847	0.688140
AN03	-70.35	-26.82	24.917111	6.825964	3.073016	0.410108	0.075518	0.896204
AN04	-69.77	-27.12	23.752575	3.466989	0.418492	2.350840	0.504247	5.377668
AN05	-70.91	-27.39	27.817124	9.829896	-7.648198	0.584264	0.136266	1.377230
AN06	-71.06	-28.97	19.384890	7.601511	-6.087159	0.459010	0.075848	1.035022
AN07	-70.45	-27.97	18.226961	10.528874	-0.186602	0.644256	0.093566	1.671938
AN08	-71.02	-27.67	23.178066	11.997874	2.706748	0.414836	0.075778	0.853212
AN10	-70.33	-26.52	27.936132	6.677065	3.609313	0.421367	0.085149	0.949013
AN13	-70.04	-26.31	28.941195	6.058689	-2.085740	0.927247	0.185212	1.854338
AN14	-70.19	-25.30	35.295128	7.344046	8.526160	2.986260	0.386831	6.574842
AN15	-69.22	-25.35	27.967717	4.895237	0.612727	0.448588	0.091870	0.944882
AN19	-69.59	-25.17	30.514829	4.886004	3.693225	0.582878	0.133059	1.256232
AN20	-70.49	-25.41	33.520000	10.360000	0.200000	1.020000	2.188388	3.303622
BESC	-69.09	-24.28	31.505201	2.591475	-63.925929	0.194531	0.341631	0.366445
BN02	-70.41	-23.67	33.329438	10.894114	4.231529	0.663170	1.110532	1.150079
BN03	-70.33	-27.37	22.353903	9.772799	-2.297140	0.147531	0.252913	0.308541
BTON	-71.49	-30.26	2.228960	5.611729	4.930190	0.565044	0.889431	1.081722
CBAA	-68.45	-22.75	21.178550	5.923876	1.603012	0.136105	0.263599	0.281991
CIFU	-70.65	-25.65	35.060804	11.206795	-5.760860	0.380083	0.607084	0.611312
CMPN	-70.69	-29.03	15.966067	4.765275	1.243352	0.136309	0.300256	0.345582

Table S1. Continuation of Table S1 (part 2/4).

Name	Lon(°)	Lat(°)	VelEW	VelNS	VelUP	ErrEW	ErrNS	ErrUP
CNBA	-71.46	-31.40	17.211297	10.408051	-2.811375	0.141649	0.302801	0.381432
COBA	-69.59	-24.82	30.178677	5.773493	3.619397	0.415277	0.088427	0.849780
CRIS	-70.39	-24.17	33.150303	9.228276	3.519444	0.127973	0.233530	0.261622
CRZL	-71.41	-29.10	19.642539	10.446202	-2.857993	0.771716	1.425105	1.735513
EMAT	-71.66	-31.15	25.398349	8.281195	-11.000319	0.323326	0.510968	0.613849
FMCO	-70.69	-26.58	28.136402	12.071425	0.420987	0.078577	0.146560	0.163928
FNKE	-69.87	-25.84	30.139516	6.649667	4.420829	0.519451	0.106808	1.007493
HSCO	-71.23	-28.46	28.493413	8.939163	-0.951358	0.146402	0.297690	0.338268
ICHA	-71.57	-29.03	27.578156	13.237521	-8.804968	0.484094	0.085303	1.036565
IDMA	-71.53	-29.23	20.942764	11.997955	-2.376078	0.352910	0.062847	0.745852
INCA	-69.91	-26.75	24.170000	4.680000	5.080000	0.840000	0.105043	1.159274
IST1	-71.42	-28.82	28.667071	10.981661	-9.576299	0.361579	0.066059	0.770297
IST2	-71.26	-29.35	13.521299	8.684892	-3.199694	0.452496	0.069780	0.913558
IST3	-70.79	-26.84	24.245974	10.904362	-0.375329	0.628143	0.121316	1.290470
IST4	-71.01	-28.69	22.382880	7.238194	-0.611914	0.444172	0.102433	0.940603
IST5	-70.56	-27.18	19.705244	10.333406	1.217085	2.260400	0.441759	4.502229
IST6	-70.21	-27.14	24.495211	6.638415	-2.583881	0.555398	0.110539	1.114200
IST7	-70.14	-27.80	19.280028	7.817002	1.196791	0.524523	0.098638	1.022172
IST8	-70.83	-27.95	21.161193	8.622563	-4.931084	2.375060	0.475035	5.093210
IST9	-71.01	-29.66	7.958394	5.363358	-1.634023	0.410735	0.084957	1.004306
JRGN	-70.57	-23.29	35.290168	11.010665	-3.737087	0.104083	0.196779	0.208887
JUNT	-70.09	-29.98	3.342403	3.414834	0.394715	0.111962	0.282775	0.288333

Table S1. Continuation of Table S1 (part 3/4).

Name	Lon(°)	Lat(°)	VelEW	VelNS	VelUP	ErrEW	ErrNS	ErrUP
LLCH	-71.08	-28.19	28.186605	9.760279	2.306307	0.111751	0.226350	0.269940
LSCH	-71.25	-29.91	2.077442	5.213429	-1.359906	0.074431	0.151163	0.184613
LVIL	-71.51	-31.91	11.289362	3.571414	-1.067607	0.444630	0.829025	1.122573
MCLA	-70.25	-22.75	30.532028	8.956578	2.879174	0.055594	0.107928	0.113785
MFLA	-69.98	-28.12	18.600099	7.260790	4.118417	0.621100	0.098842	1.168794
MRCG	-69.13	-26.84	24.109223	4.811668	3.842225	0.134631	0.283380	0.349486
OVLL	-71.20	-30.60	4.861136	7.631467	1.721002	0.129087	0.255196	0.317674
PAPO	-70.50	-25.11	31.471479	8.389665	-0.792422	1.033880	1.613328	1.712229
PAZU	-70.60	-26.15	31.823535	10.333990	0.392073	0.054139	0.118275	0.136014
PB19	-69.30	-23.90	25.049386	5.187942	3.362499	0.154132	0.250608	0.263034
PFRJ	-71.64	-30.68	8.086998	5.651351	-2.549148	0.113933	0.231254	0.308256
PMEJ	-70.45	-23.10	33.403853	10.477763	-5.051707	0.098291	0.207194	0.209452
PVCA	-71.62	-30.27	1.860660	3.804159	4.929576	0.175452	0.315806	0.383524
SLM1	-70.97	-32.04	13.369970	8.031798	4.347589	0.320269	0.489519	0.631631
SPAT	-68.18	-22.95	19.873330	5.421448	0.921263	0.121795	0.222915	0.238234
SRGD	-69.35	-22.87	27.993285	7.669316	2.122891	0.149753	0.282650	0.301879
TAMR	-70.23	-27.59	18.330794	7.857930	-4.337807	0.940448	1.989879	1.975550
UDAT	-70.35	-27.36	24.019574	9.749079	0.482341	0.179147	0.325274	0.354740
VALL	-70.76	-28.57	21.910315	5.259638	3.371130	0.589161	1.242904	1.441357
VLZL	-69.96	-23.12	30.095498	7.260971	6.117140	0.285525	0.487641	0.528059
BIN3	-70.86	-27.13	28.085323	10.264903	-7.324706	1.349450	1.390960	5.347618
CGUA	-69.59	-25.16	30.700372	6.657937	7.795010	1.179030	1.170903	5.112337

Table S1. Continuation of Table S1 (part 4/4).

Name	Lon(°)	Lat(°)	VelEW	VelNS	VelUP	ErrEW	ErrNS	ErrUP
JCHL	-68.75	-30.24	3.399014	5.597454	0.793213	0.379864	0.404511	1.551587
MCL1	-70.25	-22.75	32.201422	9.757256	-6.672040	2.717060	4.580216	18.417255
RODE	-69.13	-30.21	4.472036	4.680493	0.600372	0.572688	0.623957	2.443695
TAM3	-70.23	-27.59	13.718573	7.671846	5.982018	2.051720	0.693322	3.680167
TOCA	-69.44	-30.66	2.005987	5.116764	-0.304760	0.908983	0.982289	3.833377
SOCM	-68.29	-24.45	14.578557	0.913811	7.138825	0.391606	0.374456	1.635215